

UNDERSTANDING POLARIZATION AS A FOREGROUND FOR HI EPOCH OF  
REIONIZATION MEASUREMENTS

Saul Aryeh Kohn

A DISSERTATION

in

Physics and Astronomy

Presented to the Faculties of the University of Pennsylvania

in Partial Fulfillment of the Requirements for the Degree of Doctor of Philosophy

2018

Supervisor of Dissertation

Graduate Group Chairperson

---

James E. Aguirre  
Associate Professor of Physics and Astronomy

---

Whoever the graduate chair is  
Professor of Physics and Astronomy

Dissertation Committee:

Adam Lidz, Associate Professor of Physics and Astronomy

Masao Sako, Associate Professor of Physics and Astronomy

another professor, Assistant Professor of Physics and Astronomy

another professor, Professor of Physics and Astronomy

*for my grandparents, endless sources of inspiration*

UNDERSTANDING POLARIZATION AS A FOREGROUND FOR HI EPOCH OF  
REIONIZATION MEASUREMENTS

© COPYRIGHT

2018

Saul Aryeh Kohn

This work is licensed under the

Creative Commons Attribution

NonCommercial-ShareAlike 3.0

License

To view a copy of this license, visit

<http://creativecommons.org/licenses/by-nc-sa/3.0/>

# Acknowledgments

Acknowledgements require a certain mindset to be written well.

**ABSTRACT**

UNDERSTANDING POLARIZATION AS A FOREGROUND FOR HI EPOCH OF  
REIONIZATION MEASUREMENTS

Saul A. Kohn

James E. Aguirre

Abstracts are written last.

# Contents

<b>Title</b>	<b>i</b>
<b>Dedication</b>	<b>ii</b>
<b>Acknowledgments</b>	<b>iv</b>
<b>Abstract</b>	<b>v</b>
<b>List of Tables</b>	<b>ix</b>
<b>List of Figures</b>	<b>x</b>
<b>I Introduction &amp; Mathematical Formalisms</b>	<b>1</b>
<b>1 The Epoch of Reionization</b>	<b>2</b>
<b>2 Astrophysical Polarization</b>	<b>3</b>
<b>3 Interferometry</b>	<b>4</b>
<b>4 Instrumental Polarization</b>	<b>5</b>
<b>5 Instruments</b>	<b>6</b>
5.1 Instruments used in this work . . . . .	7
5.1.1 The Donald C. Backer Precision Array for Probing the Epoch of Reionization (PAPER) . . . . .	7
5.1.1.1 PAPER-32 redundant array . . . . .	7
5.1.1.2 PAPER-32 polarized imaging array . . . . .	7
5.1.1.3 PAPER-64 . . . . .	7
5.1.1.4 PAPER-128 . . . . .	7
5.1.2 The Hydrogen Epoch of Reionization Array (HERA) . . . . .	7
5.1.2.1 HERA-19 Commissioning Array . . . . .	7
5.1.2.2 HERA-47 . . . . .	7

5.1.2.3	Future HERA Build-Outs . . . . .	7
5.2	Other current and future low-frequency interferometers . . . . .	7
5.2.1	The Low Frequency Array (LOFAR) . . . . .	7
5.2.2	The Murchinson Widefield Array (MWA) . . . . .	7
5.2.3	Square Kilometer Array – Low band (SKA-Low) . . . . .	7
<b>II</b>	<b>Outer space in Fourier space</b>	<b>8</b>
<b>6</b>	<b>Peering through the EoR Window</b>	<b>9</b>
<b>7</b>	<b>Data Preparation and Processing</b>	<b>10</b>
7.1	Data Compression . . . . .	10
7.1.1	Delay–Delay-Rate Filtering . . . . .	11
7.1.2	Software Implementation . . . . .	13
7.2	Radio Frequency Interference . . . . .	15
7.2.1	PAPER-128 . . . . .	15
7.2.1.1	Average Properties . . . . .	16
7.2.1.2	Individual Properties . . . . .	23
7.2.1.3	Discussion . . . . .	26
7.2.2	HERA-19 and PAPER-19 . . . . .	27
7.2.2.1	HERA Hex RFI . . . . .	27
7.2.2.2	PAPER Hex RFI . . . . .	30
7.2.2.3	Hex-to-Hex Comparisons . . . . .	30
7.2.2.4	Comparison PAPER-128 stacked flags . . . . .	32
7.2.2.5	Discussion . . . . .	33
7.3	Pre-Redundant Calibration QA . . . . .	34
7.4	Post-Redundant Calibration QA . . . . .	34
<b>8</b>	<b>Polarimetric Calibration</b>	<b>35</b>
8.1	Redundant Calibration . . . . .	35
8.2	Imaging Calibration . . . . .	35
<b>9</b>	<b>The Ionosphere</b>	<b>36</b>
<b>10</b>	<b>A view of the EoR window from the PAPER-32 imaging array</b>	<b>37</b>
10.1	Observations & Reduction . . . . .	38
10.1.1	Calibration . . . . .	39
10.1.1.1	Initial calibration . . . . .	39
10.1.1.2	Absolute Calibration . . . . .	39
10.1.1.3	Polarimetric factors . . . . .	41
10.1.2	Creating power spectra . . . . .	43

<b>11 A view of the EoR window from the HERA-19 commissioning array</b>	<b>48</b>
<b>12 Deep integrations with PAPER-128</b>	<b>49</b>
<b>III Expanding the potential of EoR measurements</b>	<b>50</b>
<b>13 Time-Averaged Visibilities</b>	<b>51</b>
<b>14 Higher-order correlation functions between the kSZ and 21cm fields during the EoR</b>	<b>52</b>
<b>15 Deep Learning for 21cm Observations</b>	<b>53</b>
<b>16 Conclusions</b>	<b>54</b>
<b>Appendices</b>	<b>55</b>
<b>A Software</b>	<b>56</b>
A.1 Astronomical Interferometry in Python (aipy) . . . . .	56
A.2 Astronomy in Python (astropy) . . . . .	57
A.3 Common Astronomy Software Applications (CASA) . . . . .	57
A.4 Deep Learning packages . . . . .	57
A.5 Hierarchical Equal Area isoLatitude Pixelization of the sphere (HEALPix)	57
A.6 pyuvdata . . . . .	58
A.7 The Scientific Python Ecosystem (scipy) . . . . .	58
<b>Bibliography</b>	<b>59</b>



# List of Tables

7.1	PAPER-128 RFI frequencies and brief characterization for the averaged flags. . . . .	18
7.2	RFI as flagged by HERA . . . . .	29
7.2	RFI as flagged by HERA . . . . .	30
7.3	RFI as flagged by the PAPER Hex . . . . .	31

# List of Figures

7.1	The schema of the database used to organize and implement PAPER data compression. . . . .	14
7.2	A waterfall plot of RFI flags averaged over 150 days of PAPER-128 data. . . . .	19
7.3	The percentage of time that each frequency was flagged over the season. . . . .	20
7.4	Possible FM radio contamination. . . . .	21
7.5	Flights from Cape Town to Johannesburg correspond to RFI in the $120.15 \pm 0.35$ MHz channels. . . . .	22
7.6	The temporal profile of the 5 RFI frequencies with unidentified causes. . . . .	24
7.7	Waterfalls of RFI flags for nights 2456732, 2456958 and 2457038. . . . .	25
7.8	Waterfalls of RFI flags for nights 2456898, 2456924 and 2456965 . . . . .	25
7.9	Frequency vs. percentage flagging for the HERA Hex and PAPER Hex. . . . .	32
7.10	RFI flag waterfalls of frequency vs. South Africa Standard Time for the HERA Hex and PAPER Hex. . . . .	33
10.1	The PAPER-32, dual-pol antenna imaging configuration and $uv$ distribution. . . . .	44
10.2	Snapshot images of Stokes parameters before and absolute calibration. . . . .	45
10.3	The values of ionospheric RM for different lines of sight a range of LSTs. . . . .	46
10.4	The absolute value of delay-transformed visibilities over the bandwidth (146–166 MHz) used to create the power spectra shown in this Chapter. . . . .	47

# **Part I**

## **Introduction & Mathematical Formalisms**

# **Chapter 1**

## **The Epoch of Reionization**

## **Chapter 2**

# **Astrophysical Polarization**

# **Chapter 3**

## **Interferometry**

## **Chapter 4**

# **Instrumental Polarization**





# **Chapter 5**

## **Instruments**

### **5.1 Instruments used in this work**

#### **5.1.1 The Donald C. Backer Precision Array for Probing the Epoch of Reionization (PAPER)**

##### **5.1.1.1 PAPER-32 redundant array**

##### **5.1.1.2 PAPER-32 polarized imaging array**

##### **5.1.1.3 PAPER-64**

##### **5.1.1.4 PAPER-128**

#### **5.1.2 The Hydrogen Epoch of Reionization Array (HERA)**

##### **5.1.2.1 HERA-19 Commissioning Array**

##### **5.1.2.2 HERA-47**

##### **5.1.2.3 Future HERA Build-Outs**

### **5.2 Other current and future low-frequency interferometers**

7

#### **5.2.1 The Low Frequency Array (LOFAR)**

#### **5.2.2 The Murchinson Widefield Array (MWA)**

## **Part II**

### **Outer space in Fourier space**

## **Chapter 6**

### **Peering through the EoR Window**

# Chapter 7

## Data Preparation and Processing

The data volume of interferometric measurements inherently scale as the square of the number of antennas in the array ( $N_{\text{ant}}$ ). Not only does the sheer volume of data from large- $N_{\text{ant}}$  arrays pose a problem for data storage, but also it requires precise and efficient efforts to quality assure (QA) the data.

In this chapter, I will outline some of the efforts involved in data preparation, preprocessing and QA that are required for an EoR power spectrum estimate.

### 7.1 Data Compression

The PAPER-128 correlator produced 288 MIRIAD files per night. Each of these contained 8126 baselines, and each baseline contained visibilities over 1024 98 kHz frequency channels and 56 10 s time integrations. The four instrumental polarizations were in separate files. In sum, each file was 4.2 GB which meant that each night 1.2 TB of data were recorded.

In order to efficiently transport the data over Gigabit Ethernet from the Karoo Radio Quiet Zone (KRQZ) to Cape Town, and from Cape Town under transatlantic cables to Philadelphia, some compression was required. It was also required that such a compression, while lossy, did not effect the targeted cosmological signal.

### 7.1.1 Delay–Delay-Rate Filtering

The compression algorithm implemented for PAPER observations, Delay–Delay-Rate (DDR) filtering, was introduced in Parsons and Backer (2009) described in Parsons et al. (2014), and we briefly review it below.

The geometric delay of a celestial signal, originating from direction  $\hat{s}$ , incident on an interferometric baseline described by vector  $\vec{b}$ , is

$$\tau_g = |\vec{b} \cdot \hat{s}|/c \quad (7.1)$$

where  $c$  is the speed of light. This relationship implies that  $\tau_g$  is bounded for a given baseline

$$-|\vec{b}|/c \leq \tau_g \leq |\vec{b}|/c \quad (7.2)$$

Equation 7.2 therefore gives the maximum value of  $|\tau_g|$  physically meaningful for a given array – the maximum baseline length in that array, divided by  $c$ . For PAPER, the maximum baseline length is 300 m, corresponding to  $\max(|\tau_g|) = 1\mu\text{s}$ . As reviewed in Chapter 6, the delay axis may be accessed by Fourier transforming a visibility along the frequency axis. Once in delay space, power at delays larger in magnitude than  $1\mu\text{s}$  could be removed. With a sufficiently large frequency bandwidth, this would not produce aliased signal, according to the critical Nyquist rate. By using the  $1\mu\text{s}$  as a delay bound for all visibilities, the frequency axes of all compressed visibilities remained the same (reduced in number from 1024 to 203), which while sub-optimal from a compression point of view, allowed for ease of programming at later stages.

A similar geometric bound can be obtained by Fourier transforming the time axis of visibilities, provided that they were obtained in drift-scan mode (see Chapter 3). Parsons and Backer (2009) showed that the rate at which the geometric delay on an interferometric baseline changes is governed only by the position of the array on Earth, and the Earth’s rotation:

$$\dot{\tau}_g = -\frac{\omega_{\oplus} \cos \delta}{c} (b_x \sin \alpha + b_y \cos \alpha) \quad (7.3)$$

where  $\omega_{\oplus}$  is the angular frequency of the Earth's rotation,  $\alpha$  and  $\delta$  are the hour-angle and declination of a point on the celestial sphere, respectively, and  $\vec{b} = (b_x, b_y, b_z)$  is the baseline vector expressed in equatorial coordinates.

For arrays not close to the geographic poles,  $|b_y| \gg |b_x|$ , there is a maximum rate of change (corresponding to  $(\alpha, \delta) = (0, 0)$ ), producing a bound on  $\dot{\tau}_g$ :

$$-\omega_{\oplus}|b_y|/c \leq \dot{\tau}_g \leq \omega_{\oplus}|b_y|/c \quad (7.4)$$

for a 300 m East-West baseline, the maximum delay-rate is approximately  $\max(|\dot{\tau}_g|) = 0.07 \text{ ns s}^{-1}$ . This delay-rate was not Nyquist sampled by a single PAPER file: requiring the previous and next files generated for that polarization to be appended on either side of each visibility's time axis to prevent aliasing from the decimation. For the large scale processing of months of data, this required a software pipeline described in Section 7.1.2.

There are also other issues with DDR compression, largely associated with instrument systematics. Delay transforms rely on the fact that the bright foregrounds that dominate the measured signal are spectrally smooth, and that the frequency response of the instrument is also spectrally smooth: this of course is the basis for the EoR window paradigm reviewed in Chapter 6. Likewise, delay-rate filtering assumes temporal smoothness. Radio Frequency Interference (RFI) signals created by human communications violate both models of smoothness, since they are typically confined to narrow bandwidths (creating sharp spikes along the frequency axis) and may be transient (creating sharp spikes along the time axis). This requires steadfast identification and flagging algorithms for RFI (see Section 7.2), and some variety of interpolation, fitting, or CLEANing across the flagged regions prior to compression.

By DDR filtering of PAPER-128 data using a 300 m baseline to set the width of the filters we were able to reduce the volume of the data by an approximate factor of 70.

### 7.1.2 Software Implementation

The first season of PAPER-128 data, due to a variety of circumstances, required compression on the computing cluster at the University of Pennsylvania. The raw data were stored on a high-volume drive that was able to connect with the cluster via a low-speed switch. The hardware capable of performing any sort of high-performance processing (i.e. holding the data in RAM) were ten “compute nodes” connected to the cluster via a high-speed switch, and mounted in an NFS architecture. The compute nodes could only hold  $\sim 10$  PAPER-128 files in storage.

The processing stages for compression of a night of PAPER data, described below, required knowledge of the location and compression state of not only individual files, but also the neighbors-in-time of the file in question, in order to implement the DDR filter described above. To supervise the compression we created a MySQL database, which we interacted with via Shell and Python scripts. The database contained a table for the data files under processing and their compression state, a table of neighbor-relations, a table of file details, and a table of the processing nodes available. The schema of this database is shown in Figure 7.1.

To implement the compression, per file, the following steps were required:

1. Copying the file from the storage volume to the cluster. For a single night of data, this required roughly 8 hours.
2. Copying the file from the cluster to the compute node. This required roughly 5 minutes.
3. Generate copy of the file, with metadata corrections. This required roughly 1 minute.
4. Delete the raw file.
5. RFI-flag the high frequency-resolution data. This required roughly 2 minutes.
6. Delete the metadata-corrected file.

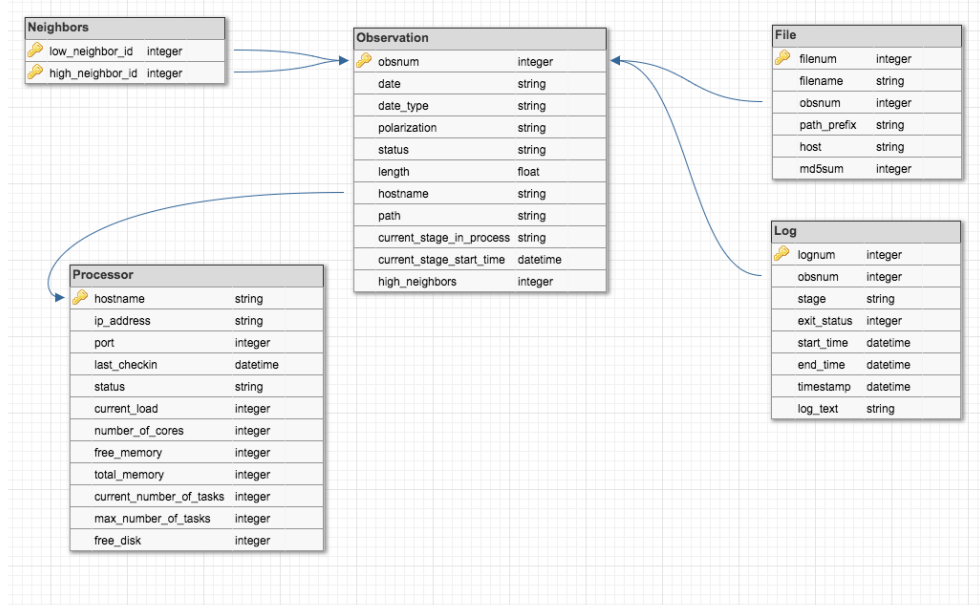


Figure 7.1: The schema of the database used to organize and implement PAPER data compression.

7. Acquire time-neighbors to the file in question, and bring them to the RFI-flagged stage. The time required for this stage varied with cluster activity, but usually required roughly 20 minutes.
8. DDR filter the RFI-flagged data, using an high-tolerance iterative CLEAN. This required roughly 20 minutes.
9. RFI flag the compressed data (coarse flagging), saving the flags to a separate file. This required roughly 1 minute.
10. Apply the coarse RFI flags to the *uncompressed*, RFI-flagged data. This required roughly one minute.
11. DDR filter the now twice-RFI-flagged data, using a low-tolerance iterative CLEAN. This required roughly 120 minutes.
12. Copy compressed data to the cluster.



13. Delete the twice-RFI-flagged data.
14. If the once-RFI-flagged data are not required as neighbors, delete them.
15. Delete the compressed data from the compute node.
16. If neighbors have already been compressed, delete them, otherwise begin their compression.
17. After all files are compressed, delete the uncompressed files from the cluster.

In total, this meant that across ten compute nodes, and efficient use of the fact that the neighbors could progress through the processing stages while the central file was being compressed, meant that it took roughly 20 to 24 hours to compress a night of observations.

## **7.2 Radio Frequency Interference**

As noted above, RFI was able to introduce spectral and temporal structure that would cause ringing in the data during compression if it was not flagged. This meant that both identification and characterization of RFI was crucial to the scientific goals of the PAPER and HERA experiments. In Section 7.2.1, I present characterization of RFI in the second season of PAPER-128 data. By averaging flags in local time I was able to investigate “repeat offender” frequency bands and identify outlying “quiet” and “loud” days. In Section 7.2.2 I analyze RFI flags from the first Internal Data Release (IDR1) of HERA commissioning data, which contained 19 HERA feeds suspended above 5 m dishes in a close-packed hexagon, and 19 PAPER feeds in the same positions as the central dishes, allowing us to investigate the difference in flagging between feeds at different altitudes.

### **7.2.1 PAPER-128**

The PAPER-128 2014 observation season ran from 18th June 2014 through the 30th April 2015. During this run, some 150 nights of data were recorded. A “night”, which I will

refer to using the JD at the start of observations, consists of twelve hours of observation from 6pm to 6am South African Standard Time (SAST). Observations as processed by the PAPER correlator are recorded in MIRIAD uv files. These files contain visibilities for each antenna pair in the array. Each integration is 20 seconds long over 1024 frequency bins from 100 to 200 MHz. Each uv file contains 56 integrations per antenna pair, and 72 uv files are recorded per linear polarization (xx, xy, yx, yy) per night.

Early in the PAPER data compression process, visibilities are flagged for RFI. This is accomplished by the aipy script *xrfi\_simple.py*, which takes the derivative of the frequency axis of all baselines associated with a single antenna, and flags any frequencies with a derivative  $\geq 6\sigma$  above the mean. We always flag the band-edges ( $\sim 7$  MHz on each side), since these frequencies are not useful to us, and always flag the  $137 \pm 0.6$  MHz band associated with ORBCOMM satellite network transmissions. This process is repeated per integration within each uv file and stored in a Python numpy zip (npz) file. This means that any baseline associated with antenna 1 can contribute a flag to the resultant npz file, which in turn is applied to the data.

The result is 280 files of high-time and -frequency resolution files per night per linear polarization containing information about the RFI environment of the HERA site. I report on the properties of these flags in time- and frequency-space over the 2014 observation season. This section is organized it as follows: in Section 7.2.1.1, I analyse the average properties of RFI over the season by stacking flags in local time and normalizing appropriately. In Section 7.2.1.2 I address nights with particularly strange RFI properties. I discuss the implications of my findings in Section 7.2.1.3.

### 7.2.1.1 Average Properties

In order to assess the average properties of the RFI environment, I calculated a weighted average of flags over the season. Over 150 nights, one-time occurrences are washed-out beneath the 1% level, allowing me to assess persistent issues.

Nominally, each night should grant 3920 integrations-worth of flags over 1024 fre-

quency bins, per linear polarization. In reality, most of the time this holds true, but occasionally not all files are compressible (hence failing to generate flags) or observations fail to start at the correct time (so there are no data to flag). Also, in the event of an X-engine failure within the correlator, contiguous chunks of the band (in eighths, i.e. 25 MHz across) are flagged-out, usually for the rest of the night.

For this reason, I calculated a weighted average of the flags across the season, but neglected nights with correlator failures or late starts. Weights were simply the number of nights that contained that integration-bin in SAST. The resultant “flag density waterfall” is shown in Figure 7.2. The color scale is indicative of flagging frequency across the season, and line plots above and to the right of the waterfall showing the percentage of times and frequencies that were flagged, respectively.

A summary of the persistent (flagged  $\geq 1\%$  of the time per channel) RFI frequencies can be found in Table 7.2.1.1. I have investigated each frequency and tried to find the most likely source for each. In most cases, this required looking at the properties in time as well as frequency. Others were more obvious from frequency alone, e.g. the 149.8 MHz transmission frequency from the International Space Station (ISS). Still others I could not track down a convincing explanation for, and these are listed with a ‘?’. A ‘?’ next to a possible cause indicates that the listed cause is the most prevalent at that frequency, but that the temporal properties of that cause do not necessarily make sense. Many of the characterizations arise from the South African Table of Frequency Allocations (SATFA; Staatskoerant (2008)).

Figure 7.3 shows the detail of the top panel of Figure 7.2. This figure highlights the broad swath of the band from roughly 150 to 180 MHz that was, on average, clear of RFI. This roughly corresponds to 21 cm redshifts  $z = 6.9$  to  $8.5$ . This is one of the reasons that the Parsons et al. (2014) and Ali et al. (2015) limits on the 21 cm power spectrum concentrated on this redshift range – there were simply more unflagged data to average-down with. Furlanetto et al. (2006) show that the  $z \sim 8$  universe can be considered roughly coeval over an  $\sim 8$  MHz bandwidth. As such, the 30 MHz chunk could be used to

Table 7.1. PAPER-128 RFI frequencies and brief characterization for the averaged flags.

$\nu$ MHz	Flagged %	Cause (Possible)	Notes or Time (SAST) Characterization
$103 \pm 3$	100	BAND EDGE	Built-in to flagger.
$107.25 \pm 0.25$	2.6	FM radio	Constant background at 2% level
$107.55 \pm 0.05$	1.9	FM radio	Constant background at 2% level
$108.1 \pm 0.4$	9	FM radio?	Rises with time, peaking at midnight and 4am
$109 \pm 0.4$	11.5	FM radio?	Rises with time, peaking around 4am
$112.8 \pm 0.1$	1.4	Aircraft?	Constant background at 1% level
$114.05 \pm 0.85$	3.7	?1	Decreases till midnight; peak at 4am
$116.55 \pm 0.35$	2.2	?2	Peak at midnight
$120.15 \pm 0.35$	3.2	Aircraft	Roughly follows CPT↔JNB flight times
$124.95 \pm 0.35$	5.5	Aircraft	Roughly follows CPT↔JNB flight times
$130.25 \pm 0.55$	4.3	?3	Falls (7pm) and rises (3am) steeply
$131.75 \pm 0.35$	10.3	Aircraft?	Peaks at 6:30, 7:30, 8:30, 9:30, 10 and then a steep falloff
$136.05 \pm 0.45$	33.1	Radar?	Decreases over night
$137.35 \pm 0.85$	100	ORBCOMM	
$141.45 \pm 0.35$	2.1	Mobile phones?	High until 9pm, then at background 1% level
$145.85 \pm 0.45$	10.7	Amateur radio	Strong 9pm-1am – this is the official downlink for ISS-HAM
$149.75 \pm 0.55$	90.7	ISS	“Beeps”, but in stacked data peaks 2am
$175.15 \pm 0.35$	20.5	VHF TV (video)	Channel 4. Peaks at 8:30pm, then falls to background 7%
$181.15 \pm 0.15$	1.6	VHF TV (audio)	Channel 4. 2% level turns-off at 10pm
$182.15 \pm 0.35$	75	?4	Decreases until 10pm (to 15%), when it begins a slow rise again
$183.2 \pm 0.5$	89.7	VHF TV (video)	Channel 5. Rises throughout night.
$186.25 \pm 0.35$	4.6	?5	Extreme turn-off at 9:45
$189.15 \pm 0.35$	41.4	VHF TV (audio)	Channel 5. Rises throughout night.
$189.9 \pm 0.4$	100	VHF TV	Channel 6. Built-in to flagger.
$191.1 \pm 0.3$	100	VHF TV	Channel 7. Built-in to flagger.
$196 \pm 4$	100	BAND EDGE	

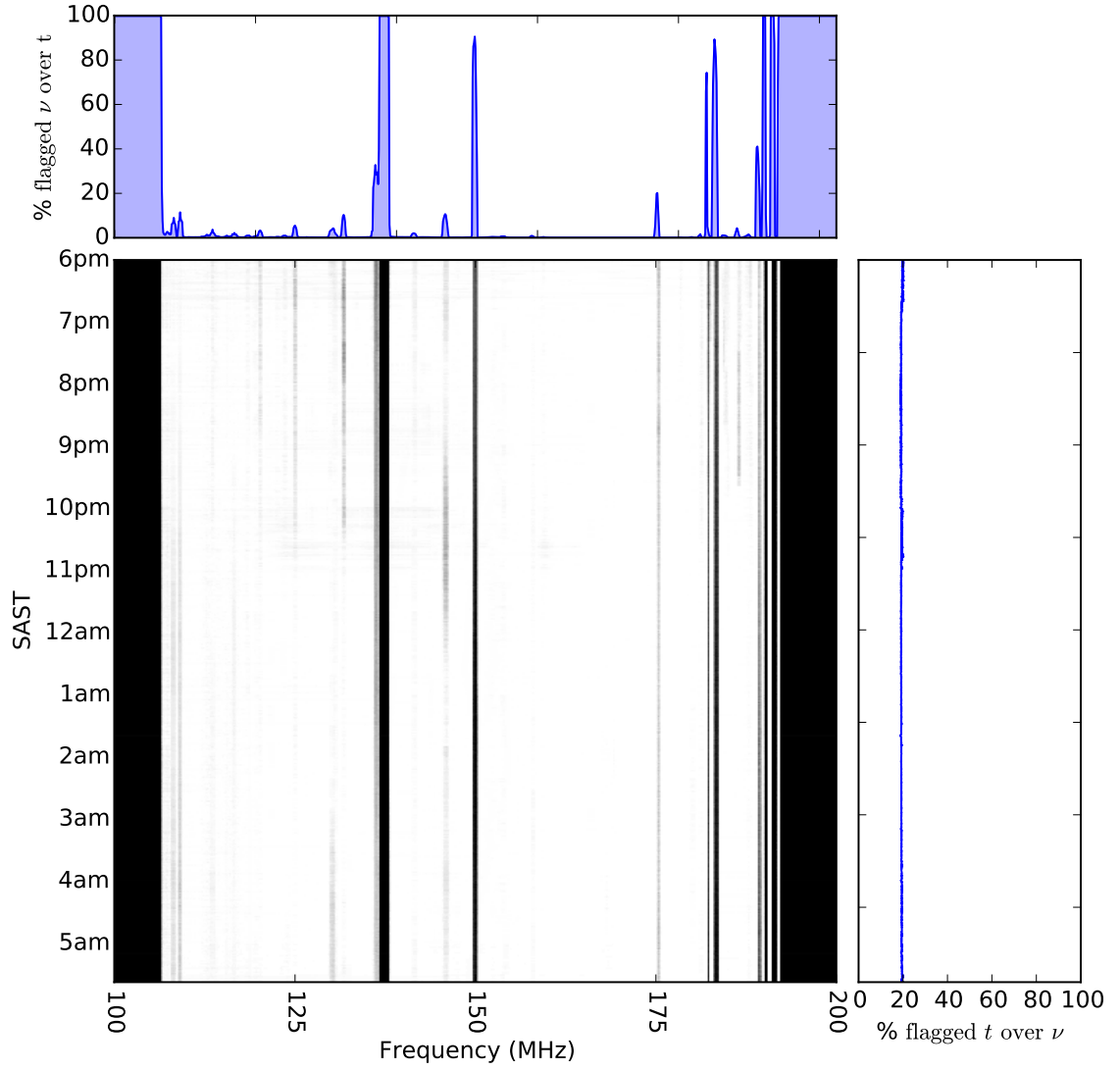


Figure 7.2: A waterfall plot of RFI flags averaged over 150 days of data. The gridding process is described in the text. Above the waterfall I show the percentage of the season each frequency is flagged, and to the right I show the percentage of frequencies that are flagged per integration.

create  $\sim 3$  power spectra, as demonstrated in Jacobs et al. (2015). As we show below, the deactivation of VHF TV broadcasts could enable measurements up to the band edge.

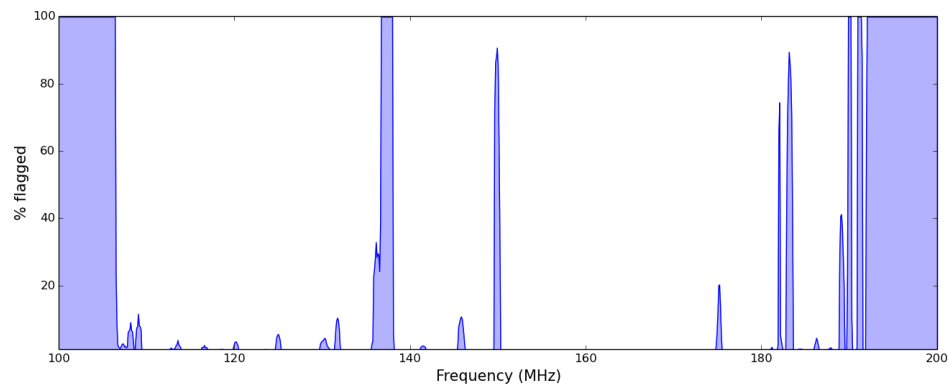


Figure 7.3: The percentage of time that each frequency was flagged over the season.

### FM Radio

SATFA lists the frequency band 87.5–108 MHz as available for FM radio broadcasts, leading me to postulate that the low-level RFI we observed in the  $107.25 \pm 0.25$  and  $107.55 \pm 0.05$  MHz bands had FM radio as the leading cause. The  $108.1 \pm 0.4$  and  $109 \pm 0.4$  MHz bands were outside of the official range, and exhibit odd temporal properties for human activity – two peaks at midnight and 4am – with a increasing number of flags throughout the average night (see Figure 7.4).

### Aircraft communications

It was difficult to argue that the  $112.1 \pm 0.1$  MHz signal is caused by aircraft communications since it maintained a constant background level. However, SATFA listed this frequency as reserved for aircraft communications and it has been used in the past as a calibration frequency for aircraft instruments South African Civil Aviation Authority (2008).

The other aircraft frequencies were obvious, because they closely traced the 2-hour

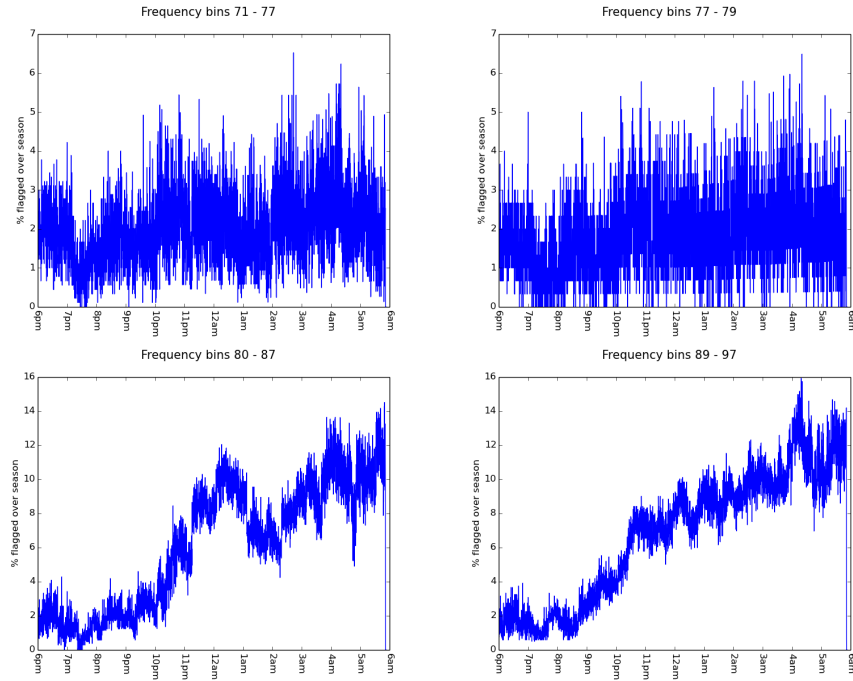


Figure 7.4: Possible FM radio contamination in the *Top, left to right*:  $107.25 \pm 0.25$  and  $107.55 \pm 0.05$  MHz bands, and *Bottom, left to right*:  $108.1 \pm 0.4$  and  $109 \pm 0.4$  MHz bands.

flight from Cape Town to Johannesburg<sup>1</sup>. An example ( $120.15 \pm 0.35$  MHz) is shown in Figure 7.5. SATFA reserved frequencies 108–117.975 MHz for aeronautical radionavigation and 117.975–137 MHz for aeronautical mobile. In Table 7.2.1.1 I listed  $131.75 \pm 0.35$  MHz as caused by aircraft since it falls in the aeronautical mobile band, but it does not follow the flight patterns as closely as the other bands.

## Orbital communications

ORBCOMM Inc.’s constellation of 29 LEO communication satellites is a well-known contaminant of the low-frequency sky, dominating over any astronomical signal at 137–138 MHz (although each satellite emits within a 20 kHz band). For this reason there was

<sup>1</sup>Credit to Danny Jacobs for first spotting this and noting it in an internal PAPER circular in December 2009.

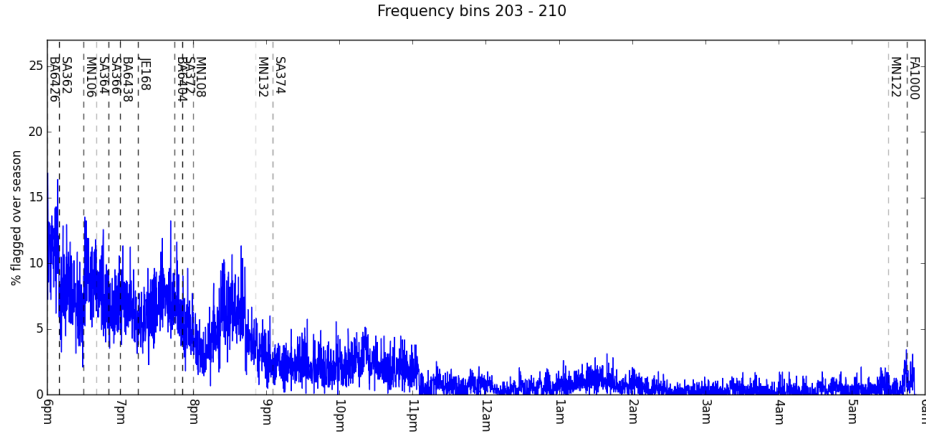


Figure 7.5: Flights from Cape Town to Johannesburg correspond to RFI in the  $120.15 \pm 0.35$  MHz channels. Vertical dashed lines indicate a flight leaving Cape Town (flights from Johannesburg are roughly concurrent) and the flight code is listed. The transparency of a line is inversely proportional to how many days a week that flight is scheduled for. The flight is 2 to 2.5 hours long – and about 2 hours after the last flight of the day, the flags fall to background level (but notably, not always to zero).

built-in flagging at  $137.35 \pm 0.85$  MHz within the compression pipeline.

The largest contaminant without built-in flags in the pipeline were communications from the ISS. The  $149.75 \pm 0.55$  MHz transmissions were semi-regular in time; they ‘beep’.

Onboard the ISS are HAM radio devices. Some countries have also launched satellites with these onboard, one of the purposes of which is to provide HAM radio operators something in space to communicate with. These devices are licensed to operate at 145.2 and 145.8 MHz, and SATFA listed the 144-146 MHz band as reserved for ‘Amateur–Satellite’ communications. We detected RFI at  $145.85 \pm 0.45$  MHz, although strong signal across  $\sim 10\%$  of the season that occurs 9pm-1am argues against human operation.

### Mobile phones and VHF TV

A weak RFI signal at  $141.45 \pm 0.35$  MHz was within the ‘mobile 1 BTX’ and aeronautical mobile band in SATFA, but other than this single listing I did not build a strong case for



the signal's cause.

VHF TV is broadcast over specifically-spaced video and audio frequencies. The strong signals at  $183.2 \pm 0.5$  MHz and  $189.15 \pm 0.35$  MHz had almost identical gradients for the percentage of flagging as a function of time of night. These frequencies corresponded exactly to Channel 5 of South African System I 625-line VHF TV signals for video and audio transmission, respectively. Similarly, the weaker signals at  $175.15 \pm 0.35$  and  $181.15 \pm 0.15$  MHz corresponded to Channel 4's video and audio transmission, respectively, but they did not share the same temporal properties.

### Unidentified sources

There were 5 RFI frequencies in the averaged data that I could not identify the sources of: weak emissions (flagged  $< 5\%$  of the season) at  $114.05 \pm 0.85$ ,  $116.55 \pm 0.35$ ,  $130.25 \pm 0.55$  and  $186.25 \pm 0.35$  MHz, and one strong emission at  $182.15 \pm 0.35$  MHz. The variation of each source with time is shown in Figure 7.6. The  $186.25 \pm 0.35$  MHz had a sharp turn-off around 9:45pm each night, suggesting that it originated from some kind of automated device.

#### 7.2.1.2 Individual Properties

Using the flags per night, I was able to assess the total number of flags as a percentage of the waterfall (i.e.  $N_{\text{flags}} / (3920 \times 1024)$ ). The average flagging per night was  $19.2 \pm 0.5\%$ , which was dominated by the permanent flagging of ORBCOMM and band edges. Four nights deviated from the average by a  $\geq 2\sigma$  excess: JDs 2456965, 2456732, 2456958 and 2457038. Their flag waterfalls are shown in Figure 7.7 (2456732, 2456958 and 2457038) and Figure 7.8 (2456965). While the strange nature of night 2456965 is discussed below, the three others followed the pattern of having strong contamination from FM and aircraft communication bands, but also had broadband 'pulses' up to about 20 minutes in length. The source of these broadband pulses is not well understood, although it was clear that

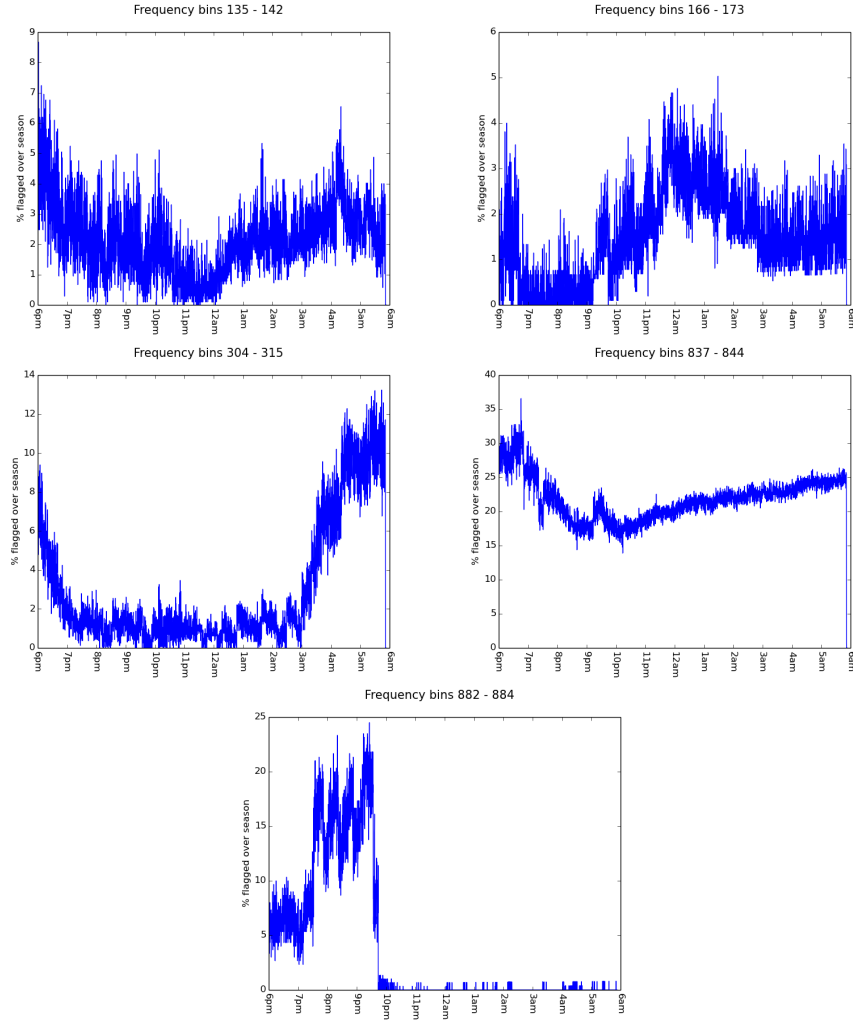


Figure 7.6: The temporal profile of the 5 RFI frequencies with unidentified causes. *Top, left to right:*  $114.05 \pm 0.85$  and  $116.55 \pm 0.35$  MHz. *Middle, left to right:*  $130.25 \pm 0.55$  and  $182.15 \pm 0.35$  MHz. *Bottom:*  $186.25 \pm 0.35$  MHz. The  $182.15 \pm 0.35$  MHz frequency is flagged a large amount of the time, making it our most-offending unidentified source.

ORBCOMM tends to spill outside of its allocated band on occasion.

JD 2456965 was easily the worst offender, and it exhibited a strange signal that wanders in frequency and time close to the ISS band. An event of note on this date (23rd November 2014) was a Soyuz FG launch that docked with the ISS – this may have been

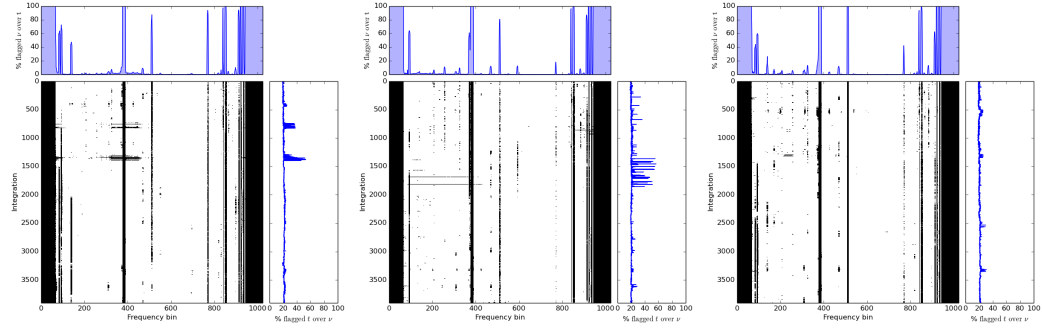


Figure 7.7: *Left to right:* waterfalls of flags for nights 2456732, 2456958 and 2457038. These three nights, along with 2456965, are  $>20.2\%$  flagged;  $> 2\sigma$  above the average flagging amount per night.

a signature of their transmissions<sup>2</sup>. Similar signals were seen on 2456898 (28th August 2014; although only at the beginning of the night) and 2456924 (23rd September 2014). There was no listed orbital or suborbital activity for 2456898. There was an US ICBM test off of the coast of Virginia on 2456924, but this was probably not the cause of the RFI. The flag waterfalls for these nights are shown in Figure ??.

Another property that the flag waterfalls in Figures 7.7 and 7.8 highlight is the presence of broadband RFI signals, typically present at frequencies lower than the ORB-COMM band. However, while we flagged at the low-end of the band (which had higher noise levels to begin with), it is likely that such broadband pulses dominated the band at those times, and that we failed to flag all of the integrations. Our flagging routine *xrft\_simple.py* does contain a thresholding option for flagging the entire integration given some arbitrary number of frequencies flagged during that integration: some experimentation will be required to decide if that threshold should change.

<sup>2</sup>The internet also suggests... less plausible explanations: <https://www.youtube.com/watch?t=11&v=VtZx8iP04zs>.

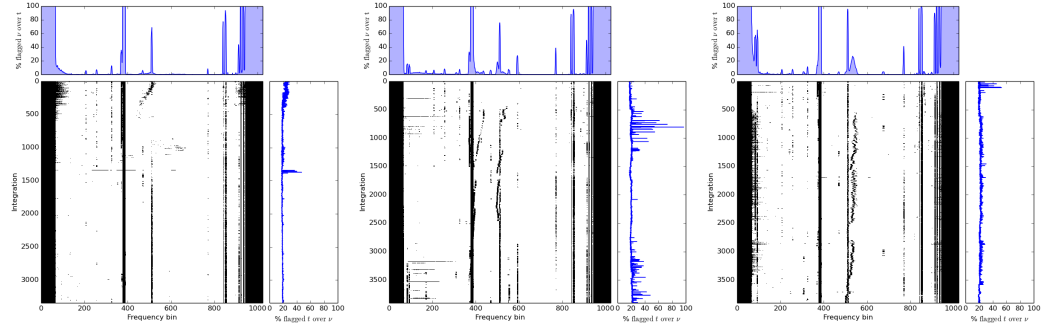


Figure 7.8: *Left to right:* waterfalls of flags for nights 2456898, 2456924 and 2456965. These three nights exhibit a strange behaviour of RFI that changes in frequency and time. JD 2456965 is by far the worst, and during this night as well as 2456898, we see a broad-band ‘comb’ of flagged frequencies near the band edges

### 7.2.1.3 Discussion

Based on my findings, I was able to recommend some actions that could be taken in the KRQZ to enable better measurements:

- Steps to reduce and ideally eliminate the VHF TV transmissions in the area would be very helpful, since these were clearly interfering with our measurements in the high-end of the band.
- The ISS  $149.75 \pm 0.55$  MHz band should be permanently flagged within the compression pipeline.
- Pursuing re-routing of flight paths will not do much to help: we see aircraft signals for the duration of their flight, not just when they’re over the Karoo.
- A lower threshold for identifying broadband RFI should be optimized.

A new, lower-frequency feed is currently under development by the HERA analog group. This would nominally allow measurements to be taken in the range 50–250 MHz, allowing science observations of the Dark Ages and the post-reionization Universe. It should be noted that at the lowest frequencies FM radio will be a constant harassment to

these measurements. At the higher frequencies, VHF TV will be the primary contaminant, but should be much easier to remove as it is both narrow-band and within the KRQZ's power to shut off.

## 7.2.2 HERA-19 and PAPER-19

The HERA-19 IDR1 consisted of four subarrays: the HERA-19 hexagon of dishes (the 'HERA Hex'), a hexagon of 19 PAPER dipoles in the exact positions of not-yet-constructed HERA dishes (the 'PAPER Hex'), an imaging array and an experimental array for polarization measurements. I will concentrate on the two Hexes in this Section. I analyzed RFI as flagged in the linear  $xx$ -polarization only. Asymmetric beams can in principle receive different RFI events for different linear polarizations, but analysis of that was outside the scope of this diagnostic study.

IDR1 consisted of one 'golden day', JD 2457458. This ran from 6pm on March 10th 2016 to 6am the following day. This gave, per baseline, roughly 4000 integrations of 10 seconds each over 1024, 100 kHz frequency channels from 100 to 200 MHz.

In order to flag RFI I used the aipy script *xrfi\_simple.py*. I took the union of all baseline flags as data to analyze. Unlike in Section 7.2.1, these data did not have a-priori flagging of band edges, which allowed me to make a more complete study of RFI in the HERA band. I did have to implement custom flags in order to get more than a zeroth-order view of the RFI (since these would dominate the flagging routine unless they are flagged already), but my results from Section 7.2.1 gave a better idea of what was flagged to get there.

Below I present measurements of high-power, mostly narrow-band RFI channels as flagged in HERA Hex data and PAPER Hex data separately. In both cases, I was able to list any channels that are flagged for  $\geq 1\%$  of the night. I could then compare the flagging Hex-to-Hex, and to PAPER-128.

### 7.2.2.1 HERA Hex RFI

Table 7.2.2.1 shows all narrowband frequency ranges flagged in HERA-19 visibilities, with columns of the frequency range in MHz, % flagging over time, plausible identification, whether or not it was identified in PAPER-128 data, and other notes (often details of the possible identification). Frequencies with 100% flagging indicate manual flags required for `xrfi_simple` to work on the rest of the channels.

Clearly, the low-end of the band was swamped by FM radio broadcasts. One notable frequency was the  $109.2 \pm 0.3$  MHz band, which was heavily flagged in HERA visibilities, but was only flagged a few percent in PAPER-128 data.

As seen before, ORBCOMM satellite emissions spilled out of their allocated 137-138 MHz band down to 136.3 MHz.

There were many narrowband RFI channels, across the band, that PAPER-128 did not pick-up. Most of these were flagged only at low levels, with two exceptions:  $111.3 \pm 0.2$  MHz and  $113.5 \pm 0.1$  MHz. Both of these were in the aircraft navigation band. There is some evidence (Civil Aviation Authority 2016) that 111.3 MHz band is for air force communications. The 113.5 MHz band is a known band for radionavigation beacons (‘VOR nav aids’) (World Aero Data 2016).

A particularly annoying ‘new’ emitter was in the  $153.8 \pm 0.2$  MHz region, which is close to the center of our nominal EoR band. It could correspond to mobile phones being used close to site.

Table 7.2. RFI as flagged by HERA

$\nu$ MHz	Flagged %	Cause (Possible)	Seen by PAPER-128	Notes
100.7 $\pm$ 0.2	50	FM Radio	n/a	RSG "Dis Die Een" Prieska
101.5 $\pm$ 0.3	36	FM Radio	n/a	RSG "Dis Die Een" Calvinia
102.4 $\pm$ 0.1	100	FM Radio	n/a	RSG "Dis Die Een" Carnarvon
102.8 $\pm$ 0.3	57	FM Radio	n/a	RSG "Dis Die Een" Pofadder
104.2 $\pm$ 0.1	100	FM Radio	n/a	SAfm Prieska
105.1 $\pm$ 0.2	100	FM Radio	n/a	SAfm Calvinia
106.2 $\pm$ 0.3	100	FM Radio	n/a	SAfm Carnarvon
106.9 $\pm$ 0.1	15	FM Radio	n/a	Sentech
107.2 $\pm$ 0.1	18	FM Radio	Yes	
107.8 $\pm$ 0.2	15	FM Radio	Yes	
108.3 $\pm$ 0.1	31	FM Radio?	Yes	
109.2 $\pm$ 0.3	93	FM Radio?	Yes...	...but not to this degree
111.3 $\pm$ 0.2	25	Air force?	No	
112.5 $\pm$ 0.1	5	Aircraft?	No	
113.5 $\pm$ 0.1	21	Aircraft	No	VOR nav aids
115.5 $\pm$ 0.1	3	Nav aids?	No	
115.9 $\pm$ 0.1	3	Nav aids?	No	
116.6 $\pm$ 0.2	9	Aircraft?	Yes	VOR-DME nav aids
120.1 $\pm$ 0.2	5	Aircraft	Yes	CPT< – >JNB
125.0 $\pm$ 0.2	6	Aircraft	Yes	CPT< – >JNB
130.0 $\pm$ 0.2	4	Aircraft	No	Communication
131.6 $\pm$ 0.2	15	Aircraft	Yes	KLM OPS
136.4 $\pm$ 0.1	9	ORBCOMM	Yes	
136.7 $\pm$ 0.1	10	ORBCOMM	Yes	
137.4 $\pm$ 0.4	100	ORBCOMM	Yes	
145.7 $\pm$ 0.4	18	ISS/Amateur Radio band	Yes	
149.9 $\pm$ 0.1	100	ISS	Yes	
153.8 $\pm$ 0.2	7	Mobile phones?	No	
175.0 $\pm$ 0.1	100	VHF TV	Yes	Channel 4 Video
178.3 $\pm$ 0.2	8	VHF TV	No	Channel 7?
181.2 $\pm$ 0.1	100	VHF TV	Yes	Channel 4 Audio
182.2 $\pm$ 0.2	9		Yes	
183.5 $\pm$ 0.6	100	VHF TV	Yes	Channel 5 Video
184.1 $\pm$ 0.1	2	VHF TV?	Yes	Channel 5?
184.7 $\pm$ 0.1	6	Broadcasting	No	
187.8 $\pm$ 0.1	4		No	
189.1 $\pm$ 0.1	52	VHF TV	Yes	Channel 5 Audio
190.1 $\pm$ 0.3	13		n/a	

Table 7.2—Continued

$\nu$ MHz	Flagged %	Cause (Possible)	Seen by PAPER-128	Notes
$191.1 \pm 0.1$	100	VHF TV	n/a	Channel 7
$197.2 \pm 0.2$	18		n/a	
$199.4 \pm 0.5$	100	BAND EDGE	n/a	

### 7.2.2.2 PAPER Hex RFI

Table 7.2.2.2 has the same description as Table 7.2.2.1, but for the PAPER Hex. There were far fewer RFI frequencies flagged in PAPER visibilities, almost all of which were seen by HERA. The only RFI seen by the PAPER Hex and not the HERA Hex was the  $123.5 \pm 0.1$  MHz emission, which I could find a plausible identification for.

### 7.2.2.3 Hex-to-Hex Comparisons

As mentioned above, the PAPER Hex saw far fewer narrowband RFI channels than HERA does. This highlighted an interesting trade-off between dipoles and dishes: at first glance, one might have expected PAPER dipoles to be more susceptible to RFI given their broader effective beams. However, HERA dipoles are lifted several meters above the ground, and this change in height may have been the source of the greater susceptibility to RFI. RFI comes from the horizon, which would be more easily received in the far sidelobes of the beam.

Even for the RFI channels they did share, HERA flagged them more often. Taking the difference in percentage-flagging for the common RFI channels (think of the left panel subtracted from the right panel for common channels in Figure 7.9), those channels had an average of 8% more flagging in HERA visibilities. The difference was particularly high in the aeronautical radionavigation bands, where HERA had on average 38% more flagging than the PAPER Hex.

Figure 7.10 shows the flags on a per-sample basis (these were averaged over time to



Table 7.3. RFI as flagged by the PAPER Hex

$\nu$ MHz	Flagged %	Cause (Possible)	Seen by PAPER-128	Notes
100.0 $\pm$ 0.1	100	BAND EDGE	n/a	
100.7 $\pm$ 0.1	11	FM Radio	n/a	RSG "Dis Die Een" Calvinia
101.6 $\pm$ 0.2	6	FM Radio	n/a	RSG "Dis Die Een" Calvinia
102.4 $\pm$ 0.1	100	FM Radio	n/a	RSG "Dis Die Een" Carnarvon
102.7 $\pm$ 0.1	100	FM Radio	n/a	RSG "Dis Die Een" Pofadder
104.2 $\pm$ 0.2	100	FM Radio	n/a	SAfm Prieska
105.1 $\pm$ 0.2	100	FM Radio	n/a	SAfm Calvinia
106.2 $\pm$ 0.3	100	FM Radio	n/a	SAfm Carnarvon
108.2 $\pm$ 0.1	3	FM Radio?	Yes	
109.1 $\pm$ 0.1	26	FM Radio?	Yes	
113.6 $\pm$ 0.1	2	Airplane Communications	No	VOR navaid
120.2 $\pm$ 0.3	3	Aircraft	Yes	CPT< – >JNB
123.5 $\pm$ 0.1	1		No	Not seen by HERA
125.0 $\pm$ 0.2	6	Aircraft	Yes	CPT< – >JNB
130.0 $\pm$ 0.3	3		No	
131.7 $\pm$ 0.2	14	Aircraft	Yes	
136.4 $\pm$ 0.2	6	ORBCOMM	Yes	
136.7 $\pm$ 0.2	6	ORBCOMM	Yes	
137.4 $\pm$ 0.4	100	ORBCOMM	Yes	
145.8 $\pm$ 0.3	14	ISS/Amateur Radio band	Yes	
149.9 $\pm$ 0.1	100	ISS	Yes	
153.8 $\pm$ 0.2	3	Single frequency mobile phones?	No	
175.1 $\pm$ 0.2	100	VHF TV	Yes	Channel 4 Video
178.3 $\pm$ 0.2	100	VHF TV	No	Channel 7?
181.2 $\pm$ 0.1	100	VHF TV	Yes	Channel 4 Audio
183.2 $\pm$ 0.2	100	VHF TV	Yes	Channel 5 Video
189.2 $\pm$ 0.1	100	VHF TV	Yes	Channel 5 Audio
191.2 $\pm$ 0.1	100	VHF TV	n/a	Channel 7
199.8 $\pm$ 0.2	100	BAND EDGE	n/a	

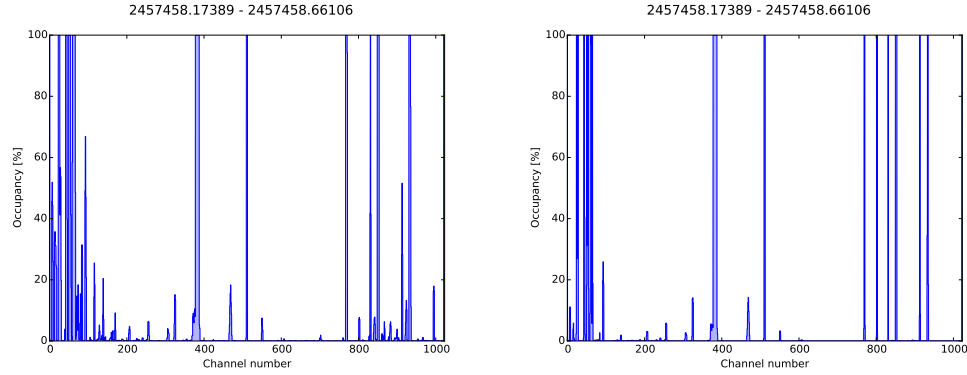


Figure 7.9: Frequency vs. percentage flagging for the HERA Hex (*left*) and PAPER Hex (*right*). Any band with greater than 1% flagging is reported in Tables 7.2.2.1 and 7.2.2.2.

create Figure 7.9). Most apparent was the occupancy of the HERA plot compared to the PAPER Hex one. An important component of this plot is the averages over frequency in the right-hand panels. We saw that the average flagging for a given time sample was about 5% higher for HERA than for the PAPER Hex, mostly due to the higher occupancy of the FM band. But we also saw something new; HERA appeared to be much more sensitive to broadband bursts of RFI. The PAPER Hex caught one of these events (around 1.30am SAST) at high significance, but most of them hardly rose above average flagging. HERA saw five to seven bursts across the night.

#### 7.2.2.4 Comparison PAPER-128 stacked flags

Section 7.2.1 presented RFI flags stacked over 150 days of observations. This method washed-out single events that effect analysis on a single-night basis, but was sensitive to repeatedly offending frequencies. Due to the PAPER-128 analysis pipeline, many channels were automatically flagged (particularly large portions of the band edges), which artificially boosted the average flagging per time and did not allow for closer inspection of the ends of the band. There was some evidence of broadband emission (see Figure 7.2) but the band was largely free of RFI in the middle of the night. Obviously, the data presented in this section shows a less-clean band, but it also only concentrated on a single

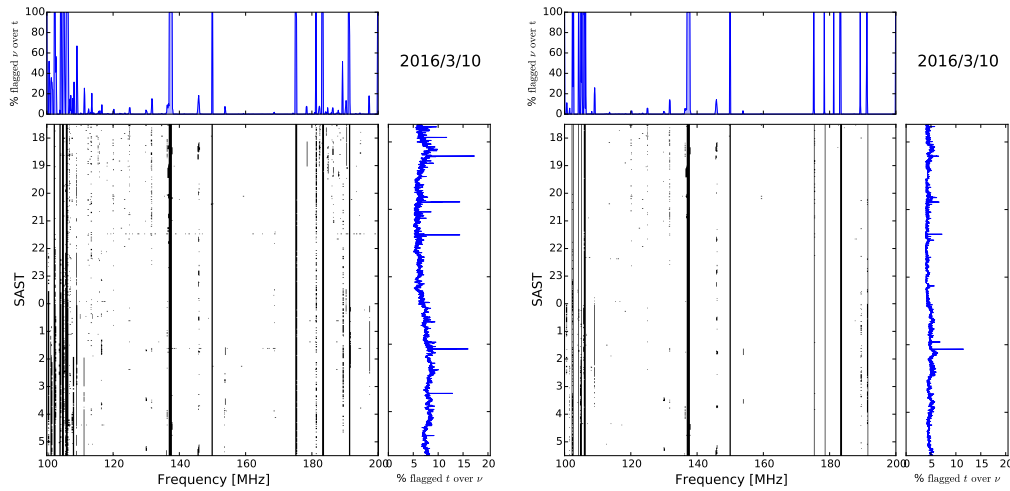


Figure 7.10: RFI flag waterfalls of frequency vs. South Africa Standard Time for the HERA Hex (*left*) and PAPER Hex (*right*). The top panels show the average over time (identical to Figure ??), while the right panels show the average over frequency.

night's data, so it may be that IDR1 was conspicuous compared to an 'average' night of observations.

Traits shared between the two analyses were:

- Aircraft communications disrupting data until around local midnight.
- ORBCOMM spilling out of it's band.
- VHF TV frequencies emitting throughout the night in the high end of the band.

Table 7.2.2.1 highlighted many frequencies seen by HERA and not by PAPER-128. Again, given the fact that flags were stacked and averaged in Section 7.2.1, these may not have been 'new', but they could have been. Particularly conspicuous were the emissions in the aeronautical radionavigation band.

### 7.2.2.5 Discussion

I have presented a first look at RFI in HERA-19 Commissioning data. Probably due to the height of the receiving element on HERA versus PAPER dipoles, much more RFI

was apparent, especially on the low and high ends of the band. Luckily, the EoR band was largely clean of RFI, except for an emitter at about 154 MHz, which could have corresponded to single-frequency mobile phone communications. Such communications are officially banned in the SKA Radio Quiet Zone (SKA Panel 2012), which HERA is in the center of.

Only looking at a single night of RFI flags limited the predictive power of this study. More data will be required to establish whether or not this level of RFI was ‘normal’. Broadband RFI bursts require closer investigation.

Efforts to extend the HERA band to lower and possibly higher frequencies are currently under way. The FM radio band extends to around 65 MHz, while the VHF TV band extends to around 230 MHz, so the RFI environment should be a consideration for these efforts.

Meanwhile, I note that the RFI flagging routine used here, `xrfi_simple`, is indeed ‘simple’. More advanced RFI flagging algorithms such as `A0Flagger` (Offringa et al. 2012) should be tested in later studies.

## **7.3 Pre-Redundant Calibration QA**

## **7.4 Post-Redundant Calibration QA**

# **Chapter 8**

## **Polarimetric Calibration**

### **8.1 Redundant Calibration**

### **8.2 Imaging Calibration**

## **Chapter 9**

### **The Ionosphere**

# Chapter 10

## A view of the EoR window from the PAPER-32 imaging array

In this Section, we present 2D power spectra created from data taken by the PAPER-32 imaging array in Stokes I, Q, U and V.

The PAPER 32-antenna array relied on its highly redundant configuration in order to take the measurements resulting in the strong upper limits on the 21 cm power spectrum (Parsons et al. 2014; Jacobs et al. 2015; Moore et al. 2017). However, for three nights in 2011 September, the 32 elements were reconfigured into an polarized imaging configuration.

Power spectra allowed us to observe and diagnose systematic effects in our calibration at high signal-to-noise within the Fourier space most relevant to EoR experiments. We observed well-defined windows in the Stokes visibilities, with Stokes Q, U and V power spectra sharing a similar wedge shape to that seen in Stokes I. With modest polarization calibration, we saw no evidence that polarization calibration errors moved power outside the wedge in any Stokes visibility, to the noise levels attained. Deeper integrations will be required to confirm that this behavior persists to the depth required for EoR detection.

The layout of this Chapter is as follows. In Section 10.1 we provide a brief description of the PAPER array in its imaging configuration, the data from which this paper is based,

and describe its calibration and reduction. We also describe the method used to create 2D power spectra in this section. We analyze the power spectra in Section ??, and discuss the implications of our findings and conclude in Section ??.

## 10.1 Observations & Reduction

We present measurements taken overnight on 2011 September 14–15 over local sidereal times (LSTs) 0–5 hr.

Antennae were arranged in a pseudo-random scatter within a 300 m-diameter circle, the layout of which is shown in Figure 10.1. This allowed us to obtain resolutions between 15' and 25' across the bandwidth (100–200 MHz nominally, although in reality this extends 110–185 MHz due to band edge effects and VHF TV). Drift-scan visibilities were measured every 10.7 s, and divided into datasets about 10 minutes in length. We express an interferometric visibility  $V_{ij}^{pq}$  between antennae  $i$  (with dipole arm  $p$ , which can be  $x$  (East-West) or  $y$  (North-South) for PAPER dipoles), and  $j$  (with dipole arm  $q$ ), in directional cosines  $l$  and  $m$  for frequency  $\nu$  at time  $t$ , as:

$$V_{ij}^{pq}(\nu, t) = g_i^p g_j^{q*} \exp(-2\pi i \nu \tau_{pq}) \times \int d\Omega A^{pq}(\Omega, \nu) S(\Omega, \nu) \exp\left(\frac{-i\nu}{c} \vec{b}(t) \cdot \hat{s}(\Omega)\right) \quad (10.1)$$

where the  $g$  terms represent the complex gains for each antenna and dipole arm,  $A^{pq}$  is the polarized beam and  $S$  is the sky. The product  $\vec{b}(t) \cdot \hat{s}(\Omega)$  represents the projection of the baseline between  $i$  and  $j$  with respect to an arbitrary location on the sky. The motivation for including the term for the delay between dipole arms  $p$  and  $q$ ,  $\tau_{pq}$ , is given in Section 10.1.1.3. This delay is clearly zero if  $p = q$ .

Visibilities were obtained from correlating both  $x$  and  $y$  dipoles, forming  $V^{xx}$ ,  $V^{xy}$ ,  $V^{yx}$  and  $V^{yy}$ . Frequencies from 100 to 200 MHz were sampled into 2048 channels. Data were delay-filtered to 203 frequency channels (see the Appendix of Parsons et al. 2014) and Chapter 7. Cross-talk was modelled and removed by subtracting the average power over



the 5 hours of observation, which extended across LST=0h–5h. An initial RFI-flagging removed any outliers more than  $6\sigma$  from a spectrally smooth profile.

### 10.1.1 Calibration

Calibration took place in three stages, detailed below: a first-order delay-space calibration for the initial gains and phases with respect to Pictor A, an absolute calibration using imaging with respect to Pictor A and Fornax A, and a polarimetric correction for the  $\tau_{xy}$  phase term in the  $V^{xy}$  and  $V^{yx}$  visibilities. Traditional polarimetric calibration proceeds by observing a source with a known polarization angle, and solving for up to seven direction-independent terms in the Jones matrix (e.g. Thompson et al. 2017; Hamaker et al. 1996), as well correcting for the effects of the primary beam. Given the dearth of suitable calibrators at our observing frequencies, especially at the relatively low resolution and sensitivity of the array, we proceeded with polarized calibration using different techniques, as described in Section 10.1.1.3 below.

#### 10.1.1.1 Initial calibration

A first-order gain and phase calibration was performed by a similar approach to Jacobs et al. (2013). Each 10 minute drift-scan dataset was phased to the known position of Pictor A using `aipy` routines.

The gain term in Equation ?? was approximated as

$$g_i^p = G_i^p \exp(-2\pi i \nu \tau_{ip}) \quad (10.2)$$

and the required delay  $\tau_{ip}$  offset of the uncalibrated delay tracks to the real position on the sky solved for to obtain a phase calibration; the absolute flux calibration  $G_i^p$  was found by isolating the tracks of Pictor A in delay space, and applying the required flux scale across the band (for a discussion of delay-space calibration, see Parsons et al. 2012b, and Figure ??).

### 10.1.1.2 Absolute Calibration

Visibilities were converted to CASA Measurement Sets to be further calibrated using a custom pipeline developed around CASA libraries. Snapshot images were generated for each 10 minute observation by Fourier transforming the visibilities. We used uniform weights and the multi-frequency synthesis algorithm to further improve the  $uv$  coverage. Dirty images were deconvolved down to a 5 Jy threshold using the Cotton-Schwab algorithm. The sky model generated by the CLEAN components was used to self-calibrate each snapshot over the full bandwidth, using a frequency-independent sky-model and averaging over the 10 minute observation. We corrected for residual cable length errors by computing antenna-based phase solutions for each frequency channel for each snapshot observation. After self-calibration, snapshot visibilities were again Fourier transformed into images and deconvolved down to a 2 Jy threshold to form the final sky models. These final sky models were used to solve for a frequency independent, diagonal, complex Jones matrix (Hamaker et al. 1996; Smirnov 2011) for each antenna in order to calibrate gain variations from snapshot to snapshot. We make no attempt to correct sky models for polarized primary beams and, therefore, our gain solutions incorporate both the direction independent and the direction dependent responses of the two gain polarizations. This is a reasonable approximation for the scope of the paper, as, eventually, wide-field polarization corrections cannot be implemented directly in the per-baseline power spectrum estimation (see Section ??).

The average correction in magnitude through this second-order calibration was a  $\pm 6\%$  change for  $x$  gains and  $\pm 7\%$  for  $y$  gains from those derived in the initial delay-space calibration. If the gain on an antenna deviated by more than 30% from image-to-image during this analysis, it was discarded from future processing stages, since it was likely malfunctioning. This was true for 3 antennae (see the top panel of Figure 10.1).

The final gain amplitude calibration was carried out similarly to Ali et al. (2015). We generated single channel images between 120 and 174 MHz for each snapshot and deconvolved each of them down to 10 Jy. For each snapshot, a source spectrum is derived

for Pictor A by fitting a two dimensional Gaussian the source using the PyBDSM<sup>1</sup> source extractor (?). Spectra were optimally averaged together by weighting them with the primary beam model evaluated in the direction of Pictor A. To fit the absolute calibration, we divided the model spectrum (Jacobs et al. 2013) by the measured one and fit a 6th order polynomial over the 120-174 MHz frequency range. This procedure was repeated using Fornax A with the only difference that a taper was applied to the visibilities (120 m) in order to reduce Fornax A to a point-like source and use the model spectrum from Bernardi et al. (2013). The best fit coefficients for Pictor A and Fornax A were averaged together to obtain the final absolute flux density calibration. Snapshots of fully CASA-calibrated data are shown in Figure 10.2.

### 10.1.1.3 Polarimetric factors

Standard full polarization calibration involves correcting for leakage of Stokes  $I$  into the  $V_{ij}^{xy}$  and  $V_{ij}^{yx}$  visibilities and leakage of polarized signal into total intensity (the so called Jones  $D$  matrices or  $D$ -terms; e.g. Thompson et al. (2017); Hamaker et al. (1996)), and an unknown phase difference between the  $x$  and  $y$  feeds (e.g. Sault et al. 1996).

We attempt no  $D$  matrix calibration in this paper, as there is not a dominant source to be used for such calibration: the limited sensitivity of our observations does not offer good signal-to-noise ratio on PMN J0351-2744, the only polarized source at low frequencies known so far in our survey area. In addition,  $D$ -term calibration would require determination of the primary beam Mueller matrices beyond our current accuracy. The consequences of this limitation are discussed in the analysis of our power spectra in Section ??.

As a intermediate measure compatible with these limitations, we therefore adopted a minimization of the phase difference between the  $V_{ij}^{xy}$  and  $V_{ij}^{yx}$  visibilities, minimizing a sum of squared weighted residuals  $w$ :

---

<sup>1</sup><http://www.lofar.org/wiki/doku.php?id=public:usersoftware:pybdsm>

$$w(\nu, t, \tau_{xy}) = \sum_{ij} |V_{ij}^{xy} - V_{ij}^{yx} \exp(-2\pi i \nu \tau_{xy})|^2 \quad (10.3)$$

to find an estimated value of  $\tau_{xy}$  for the array at each  $(\nu, t)$  sample. This is equivalent to assuming that the sky is intrinsically not circularly polarized at the frequencies observed by PAPER.

We choose not to correct for ionospheric Faraday rotation in our calibration. Not only is this difficult to do for widefield instruments, but also the ionosphere was relatively stable during the observations, so we expect little incoherent averaging during the power spectrum stage below. We calculated the stability of ionospheric RM ( $\phi_{\text{iono}}$ ) using the IONFR software (Sotomayor-Beltran et al. 2013), which calculates the  $\phi_{\text{iono}}$  for a given longitude, latitude and time by interpolating values of GPS-derived total electron content maps and the International Geomagnetic Reference Field (Finlay et al. 2010). The values of  $\phi_{\text{iono}}$  for different lines of sight are shown in Figure 10.3. Fluctuations of  $\phi_{\text{iono}}$  will cause incoherent time-averaging and subsequent loss of polarized signal. Using the formalism of ? to calculate the attenuation factor, we found that none of the lines of sight (except for the 21h,0° one which goes beneath the horizon) shown are responsible for attenuating signal by  $> 20\%$  in power-spectrum space (see Section 10.1.2).

We form linear combinations of the instrument visibilities, the so-called pseudo-Stokes visibilities (see e.g. Moore et al. 2013)  $V^I$ ,  $V^Q$ ,  $V^U$  and  $V^V$  as:

$$\begin{pmatrix} V^I \\ V^Q \\ V^U \\ V^V \end{pmatrix} = \begin{pmatrix} 1 & 0 & 0 & 1 \\ 1 & 0 & 0 & -1 \\ 0 & 1 & 1 & 0 \\ 0 & -i & i & 0 \end{pmatrix} \begin{pmatrix} V^{xx} \\ V^{xy} \\ V^{yx} \\ V^{yy} \end{pmatrix} \quad (10.4)$$

Data that were reduced, calibrated, and formed into Stokes visibilities were separated into delay spectra inside and outside of the horizon for each baseline. We used a 50 ns margin for what was considered ‘inside’ the horizon, in order to confine all supra-horizon emission (e.g. Parsons et al. 2012b; Pober et al. 2013) to the foreground component of the data. We implemented a one-dimensional CLEAN (Parsons and Backer 2009; Parsons

et al. 2012a) with a Blackman-Harris window to a tolerance of  $10^{-9}$ . RFI is more easily identified in foreground-removed data, so we RFI-flagged again on the background data deviations greater than  $3\sigma$ . We then added the inside- and outside-horizon visibilities back together; RFI flags were preserved in the process.

The effect of our calibration is shown in the delay-transformed visibilities in Figure 10.4. As is apparent in Figure 10.2, after improved calibration there are fewer delay tracks (i.e. sources) in the Stokes Q visibilities, while there is little overall change in Stokes U. The minimization of Stokes V, performed after the imaging calibration stage, moves power from Stokes V into Stokes U, effectively accounting for part of a  $D$ -term correction. But without an accurate  $D$ -term calibrator, Stokes U exhibits additional (and dominant)  $D$ -term leakage from Stokes I, in this case due to Pictor A. Pictor A is the brightest source in Stokes I in our observed field, and thus dominates the visibility shown. There is no reason to suppose that Pictor A is pure Stokes U (compare also Figure 10.2), and thus the bulk of this emission must be leakage.

### 10.1.2 Creating power spectra

Expressing the visibility  $V_{ij}^{pq}(\nu, t)$  observed at time  $t$  (see Equation 10.1) in terms of the geometrical delay  $\tau_g = \vec{b}(t) \cdot \hat{s}(l, m)/c$  for the baseline  $ij$ , Parsons et al. (2012b) define the delay transform as the Fourier transform of the visibility along the frequency axis:

$$\tilde{V}_{ij}^{pq}(\tau, t) = \int d\nu V_{ij}^{pq}(\nu, t) e^{2\pi i \nu \tau} \quad (10.5)$$

We can represent the power at each frequency and baseline in an array as a power spectrum in terms of their respective Fourier components  $k_{\parallel}$  and  $k_{\perp}$  as:

$$P(k_{\parallel}, k_{\perp}) \approx |\tilde{V}_{ij}^{pq}(\tau, t)|^2 \frac{X^2 Y}{\Omega B} \left( \frac{c^2}{2k_B \nu^2} \right)^2 \quad (10.6)$$

where  $B$  is the bandwidth,  $\Omega$  is the angular area (i.e. proportional to the beam area), and  $X$  and  $Y$  are redshift-dependent scalars calculated in Parsons et al. (2012a).

To form  $|\tilde{V}_{ij}^{pq}(\tau, t)|^2$ , consecutive integrations were cross-multiplied, phasing the zenith of latter to the former i.e.:

$$|\tilde{V}_{ij}^{pq}(\tau, t)|^2 \approx |V_{ij}^{pq}(\tau, t) \times V_{ij}^{pq}(\tau, t + \Delta t) e^{i\theta_{ij, \text{zen}}(\Delta t)}|^2 \quad (10.7)$$

where  $\Delta t=10.7$  seconds and  $\theta_{ij, \text{zen}}(\Delta t)$  is the appropriate zenith rephasing factor. This method should avoid noise-biased power spectra except on very long baselines, which the PAPER configuration does not contain, while sampling essentially identical  $k$ -modes. Note that this is the same method used by Pober et al. (2013) in their investigation of the unpolarized wedge.

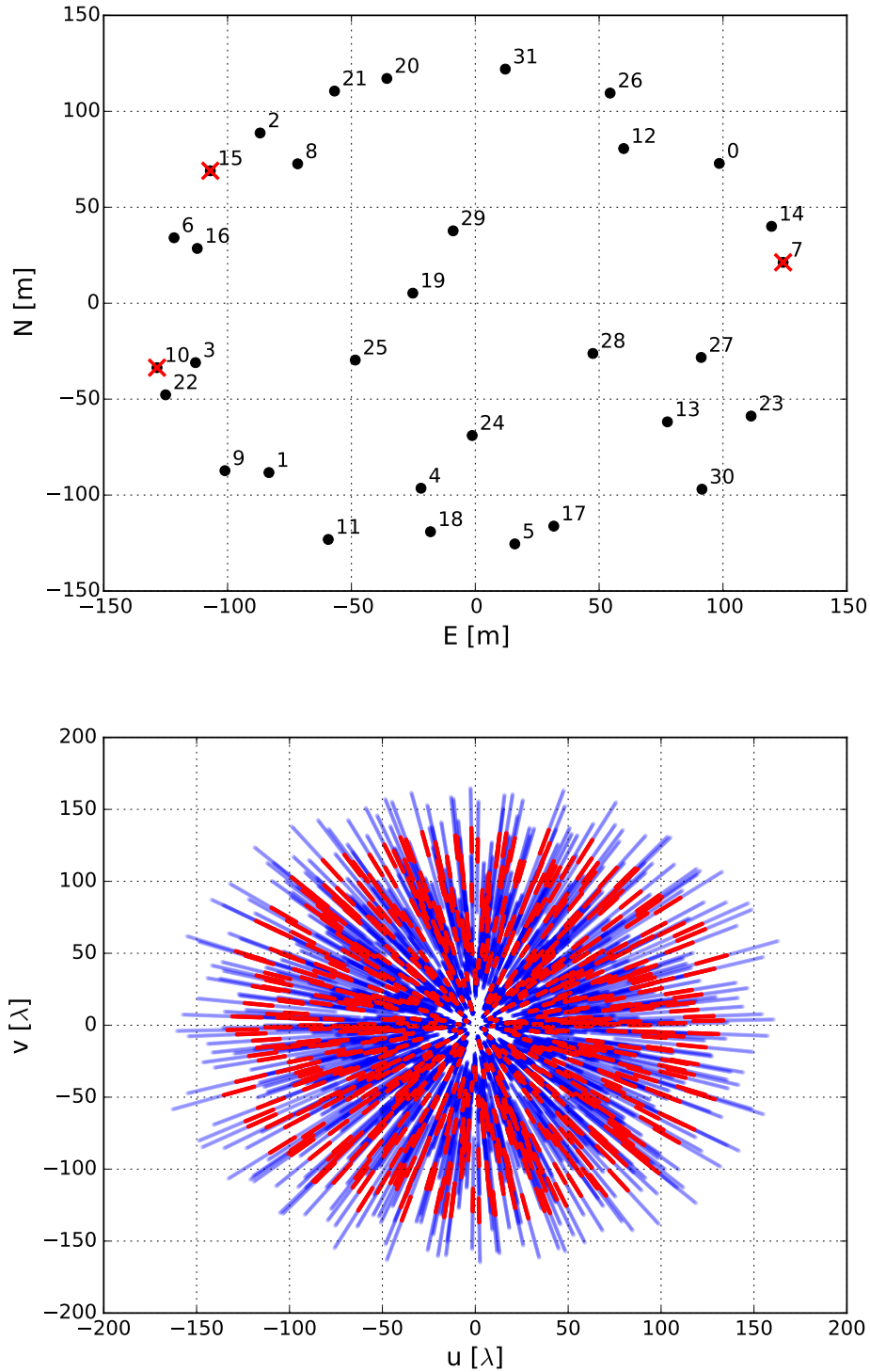


Figure 10.1: The PAPER-32, dual-pol antenna imaging configuration (top). They were arranged in a pseudo-random scatter within in a  $\sim 300$  m diameter circle to maximize instantaneous  $uv$  coverage (bottom).  $uv$  coverage is shown for 100–200 MHz over 203 channels in blue, and 146–166 MHz over 20 channels in red (the latter being the frequencies used in our power spectrum analysis). Malfunctioning antennae identified during calibration are overlaid with red crosses (and are excluded from the  $uv$  coverage map).

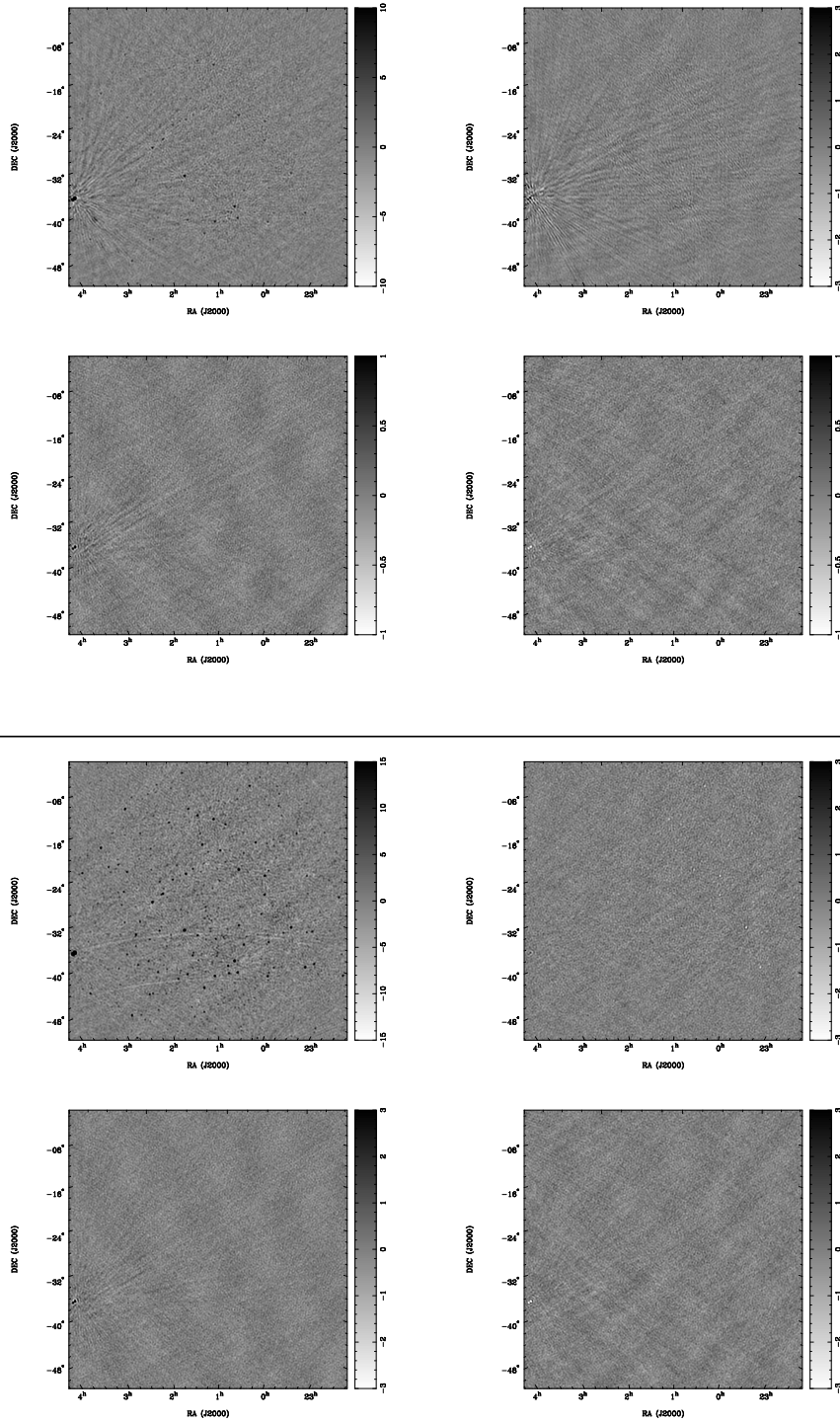


Figure 10.2: *Above:* Example of a Stokes I snapshot image (top left) with corresponding Stokes Q (top right), Stokes U (bottom left) and Stokes V (bottom right) images before absolute calibration. *Below:* The same organization as above, after absolute calibration. No primary beam correction was applied. The Stokes I image was deconvolved down to  $5 \text{ Jy beam}^{-1}$  whereas the other images were not deconvolved. We note that the Stokes Q image is relatively featureless apart from a few faint sources that appear instrumentally polarized. Stokes U and Stokes V images are, instead, dominated by Fornax A that



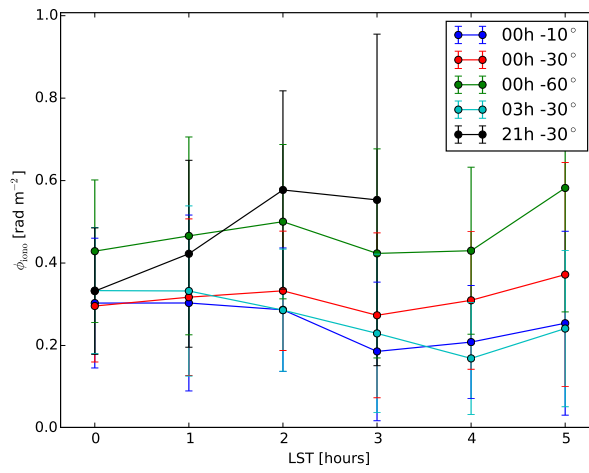


Figure 10.3: The values of ionospheric RM for different lines of sight the range of LSTs in this analysis, as calculated by IONFR (Sotomayor-Beltran et al. 2013). The 21h,0° line of sight goes beneath the horizon after LST=3h, and therefore has fewer data points.

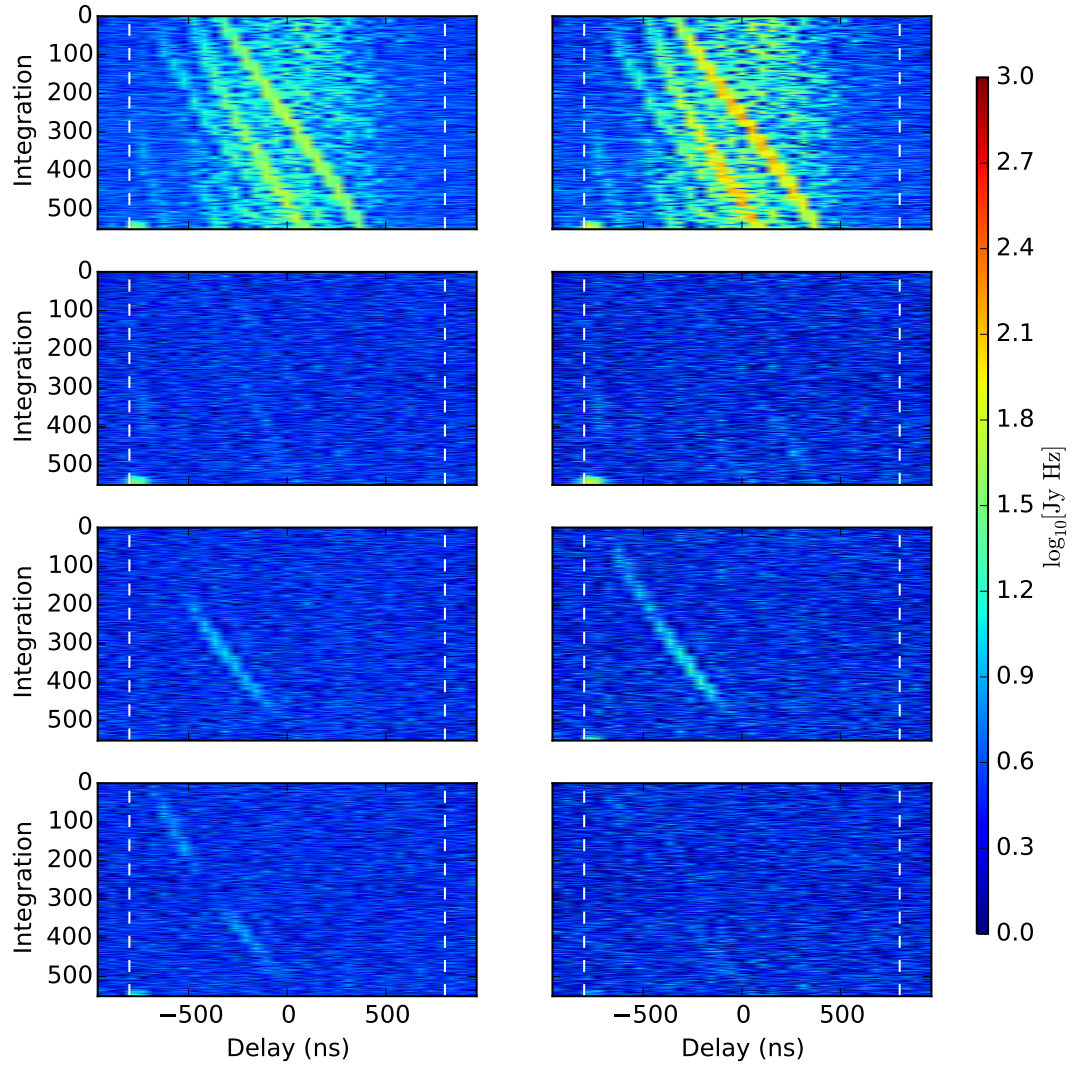


Figure 10.4: The absolute value of delay-transformed visibilities over the bandwidth (146–166 MHz) used to create the power spectra shown in this Chapter. The left and right columns show the visibilities before and after absolute calibration (and for Stokes U and V, the application of the  $\tau_{xy}$  parameter), respectively, for baseline formed by antennae 6 and 14 ( $\sim 250$  m in length, approximately East-West). The flux scale in the left column as been boosted for a more fair comparison to the absolute-calibrated data. From top to bottom, the rows correspond to Stokes I, Q, U and V. The horizon limit is marked by white dashed lines.

## **Chapter 11**

### **A view of the EoR window from the HERA-19 commissioning array**

## **Chapter 12**

### **Deep integrations with PAPER-128**

## **Part III**

# **Expanding the potential of EoR measurements**

## **Chapter 13**

### **Time-Averaged Visibilities**

## **Chapter 14**

### **Higher-order correlation functions between the kSZ and 21cm fields during the EoR**

## **Chapter 15**

# **Deep Learning for 21cm Observations**



## **Chapter 16**

## **Conclusions**

# **Appendices**

# Appendix A

## Software

Software engineering and maintenance of existing codebases has been, generally speaking, historically undervalued and unappreciated (Muna et al. 2016). In this Appendix I would like to provide a brief description of the major software packages used in this work – without which, the work would not exist.

### A.1 Astronomical Interferometry in Python (aipy)

The aipy software package (Parsons 2016) was developed by a team based largely at the University of California, Berkeley and led by Aaron Parsons. Developed under NSF funding for the PAPER experiment, it provides a Python API to interact with interferometric visibilities stored in the MIRIAD file format (Sault et al. 2011). It is able to efficiently query large MIRIAD files due to the API's closeness to the underlying C code. It also contains calibration, deconvolution, imaging and phasing code in Python, and interfaces with HEALPix (see Section A.5, below) as well as other astronomical Python packages.

aipy is maintained by the HERA software team, and can be found at: <https://github.com/HERA-Team/aipy>.

## **A.2 Astronomy in Python (astropy)**

astropy is an open-source and community-developed core Python package for Astronomy, containing a host of extremely useful utility functions and objects (Astropy Collaboration et al. 2013).

## **A.3 Common Astronomy Software Applications (CASA)**

CASA is under active development, with the primary goal of supporting the data post-processing needs of the next generation of radio telescopes. It is developed by an international consortium of scientists based at the National Radio Astronomical Observatory (NRAO), the European Southern Observatory (ESO), the National Astronomical Observatory of Japan (NAOJ), the CSIRO Australia Telescope National Facility (CSIRO/ATNF), and the Netherlands Institute for Radio Astronomy (ASTRON), under the guidance of NRAO (McMullin et al. 2007).

## **A.4 Deep Learning packages**

Experimentation with deep learning analyses of 21 cm simulated observations took place in Keras (Chollet et al. 2015), PyTorch (Paszke et al. 2017) and Tensorflow (Abadi et al. 2016).

## **A.5 Hierarchical Equal Area isoLatitude Pixelization of the sphere (HEALPix)**

The HEALPix software, and its Python wrapper healpy, provide a pixelization which subdivides a spherical surface into pixels which each cover the same surface area as every other pixel. Pixel centers occur on a discrete number of rings of constant latitude. This

scheme makes natively spherical measurements, such as angular power spectra and wide-field images, simple and efficient to interact with (Górski et al. 2005).

## A.6 pyuvdata

pyuvdata provides a Python interface to interferometric data. It can read and write MIRIAD and UVFITS file formats, as well as read CASA measurement sets and FHD (Sullivan et al. 2012) visibility save files (Hazelton et al. 2017).

pyuvdata is maintained by the HERA software team, and can be found at: <https://github.com/HERA-Team/pyuvdata>.

## A.7 The Scientific Python Ecosystem (scipy)

Many of the above tools require at least one of the many packages under the scipy ecosystem. It is truly foundational to almost any scientific analysis that takes place in Python (Jones et al. 2001).

# Bibliography

- Abadi, M., Agarwal, A., Barham, P., Brevdo, E., Chen, Z., Citro, C., Corrado, G. S., Davis, A., Dean, J., Devin, M., Ghemawat, S., Goodfellow, I., Harp, A., Irving, G., Isard, M., Jia, Y., Jozefowicz, R., Kaiser, L., Kudlur, M., Levenberg, J., Mane, D., Monga, R., Moore, S., Murray, D., Olah, C., Schuster, M., Shlens, J., Steiner, B., Sutskever, I., Talwar, K., Tucker, P., Vanhoucke, V., Vasudevan, V., Viegas, F., Vinyals, O., Warden, P., Wattenberg, M., Wicke, M., Yu, Y., and Zheng, X.: 2016, *ArXiv e-prints*
- Ali, Z. S., Parsons, A. R., Zheng, H., Pober, J. C., Liu, A., Aguirre, J. E., Bradley, R. F., Bernardi, G., Carilli, C. L., Cheng, C., DeBoer, D. R., Dexter, M. R., Grobbelaar, J., Horrell, J., Jacobs, D. C., Klima, P., MacMahon, D. H. E., Maree, M., Moore, D. F., Razavi, N., Stefan, I. I., Walbrugh, W. P., and Walker, A.: 2015, *ArXiv e-prints*
- Astropy Collaboration, Robitaille, T. P., Tollerud, E. J., Greenfield, P., Droettboom, M., Bray, E., Aldcroft, T., Davis, M., Ginsburg, A., Price-Whelan, A. M., Kerzendorf, W. E., Conley, A., Crighton, N., Barbary, K., Muna, D., Ferguson, H., Grollier, F., Parikh, M. M., Nair, P. H., Unther, H. M., Deil, C., Woillez, J., Conseil, S., Kramer, R., Turner, J. E. H., Singer, L., Fox, R., Weaver, B. A., Zabalza, V., Edwards, Z. I., Azalee Bostroem, K., Burke, D. J., Casey, A. R., Crawford, S. M., Dencheva, N., Ely, J., Jenness, T., Labrie, K., Lim, P. L., Pierfederici, F., Pontzen, A., Ptak, A., Refsdal, B., Servillat, M., and Streicher, O.: 2013, *A&A* **558**, A33
- Bernardi, G., Greenhill, L. J., Mitchell, D. A., Ord, S. M., Hazelton, B. J., Gaensler, B. M., de Oliveira-Costa, A., Morales, M. F., Udaya Shankar, N., Subrahmanyan, R., Wayth,

- R. B., Lenc, E., Williams, C. L., Arcus, W., Arora, B. S., Barnes, D. G., Bowman, J. D., Briggs, F. H., Bunton, J. D., Cappallo, R. J., Corey, B. E., Deshpande, A., deSouza, L., Emrich, D., Goeke, R., Herne, D., Hewitt, J. N., Johnston-Hollitt, M., Kaplan, D., Kasper, J. C., Kincaid, B. B., Koenig, R., Kratzenberg, E., Lonsdale, C. J., Lynch, M. J., McWhirter, S. R., Morgan, E., Oberoi, D., Pathikulangara, J., Prabu, T., Remillard, R. A., Rogers, A. E. E., Roshi, A., Salah, J. E., Sault, R. J., Srivani, K. S., Stevens, J., Tingay, S. J., Waterson, M., Webster, R. L., Whitney, A. R., Williams, A., and Wyithe, J. S. B.: 2013, *ApJ* **771**, 105
- Chollet, F. et al.: 2015, *Keras*, <https://github.com/fchollet/keras>
- Civil Aviation Authority: 2016, <http://www.caa.co.za/Pages/Search-results.aspx?k=frequency#k=113.3%20MHz>, website
- Finlay, C. C., Maus, S., Beggan, C. D., Bondar, T. N., Chambodut, A., Chernova, T. A., Chulliat, A., Golovkov, V. P., Hamilton, B., Hamoudi, M., Holme, R., Hulot, G., Kuang, W., Langlais, B., Lesur, V., Lowes, F. J., Lühr, H., MacMillan, S., Mande, M., McLean, S., Manoj, C., Menvielle, M., Michaelis, I., Olsen, N., Rauberg, J., Rother, M., Sabaka, T. J., Tangborn, A., Tøffner-Clausen, L., Thébaud, E., Thomson, A. W. P., Wardinski, I., Wei, Z., and Zvereva, T. I.: 2010, *Geophysical Journal International* **183**, 1216
- Furlanetto, S. R., Oh, S. P., and Briggs, F. H.: 2006, *Physics Review* **433**, 181
- Górski, K. M., Hivon, E., Banday, A. J., Wandelt, B. D., Hansen, F. K., Reinecke, M., and Bartelmann, M.: 2005, *ApJ* **622**, 759
- Hamaker, J. P., Bregman, J. D., and Sault, R. J.: 1996, *A&AS* **117**, 137
- Hazelton, B., Beardsley, A., Poher, J., Jacobs, D., Ali, Z., and Lanman, A.: 2017, *HERA-Team/pyuvdata: Version 1.1*

- Jacobs, D. C., Parsons, A. R., Aguirre, J. E., Ali, Z., Bowman, J., Bradley, R. F., Carilli, C. L., DeBoer, D. R., Dexter, M. R., Gugliucci, N. E., Klima, P., MacMahon, D. H. E., Manley, J. R., Moore, D. F., Pober, J. C., Stefan, I. I., and Walbrugh, W. P.: 2013, *ApJ* **776**, 108
- Jacobs, D. C., Pober, J. C., Parsons, A. R., Aguirre, J. E., Ali, Z. S., Bowman, J., Bradley, R. F., Carilli, C. L., DeBoer, D. R., Dexter, M. R., Gugliucci, N. E., Klima, P., Liu, A., MacMahon, D. H. E., Manley, J. R., Moore, D. F., Stefan, I. I., and Walbrugh, W. P.: 2015, *ApJ* **801**, 51
- Jones, E., Oliphant, T., Peterson, P., et al.: 2001, *SciPy: Open source scientific tools for Python*, [Online; accessed <today>]
- McMullin, J. P., Waters, B., Schiebel, D., Young, W., and Golap, K.: 2007, in R. A. Shaw, F. Hill, and D. J. Bell (eds.), *Astronomical Data Analysis Software and Systems XVI*, 376, p. 127, ASP, San Francisco, CA
- Moore, D. F., Aguirre, J. E., Kohn, S. A., Parsons, A. R., Ali, Z. S., Bradley, R. F., Carilli, C. L., DeBoer, D. R., Dexter, M. R., Gugliucci, N. E., Jacobs, D. C., Klima, P., Liu, A., MacMahon, D. H. E., Manley, J. R., Pober, J. C., Stefan, I. I., and Walbrugh, W. P.: 2017, *ApJ* **836**, 154
- Moore, D. F., Aguirre, J. E., Parsons, A. R., Jacobs, D. C., and Pober, J. C.: 2013, *ApJ* **769**, 154
- Muna, D., Alexander, M., Allen, A., Ashley, R., Asmus, D., Azzollini, R., Bannister, M., Beaton, R., Benson, A., Berriman, G. B., Bilicki, M., Boyce, P., Bridge, J., Cami, J., Cangi, E., Chen, X., Christiny, N., Clark, C., Collins, M., Comparat, J., Cook, N., Croton, D., Delberth Davids, I., Depagne, É., Donor, J., dos Santos, L. A., Douglas, S., Du, A., Durbin, M., Erb, D., Faes, D., Fernández-Trincado, J. G., Foley, A., Fotopoulou, S., Frimann, S., Frinchaboy, P., Garcia-Dias, R., Gawryszczak, A., George, E., Gonzalez, S., Gordon, K., Gorgone, N., Gosmeyer, C., Grasha, K., Greenfield, P.,



Grellmann, R., Guillochon, J., Gurwell, M., Haas, M., Hagen, A., Haggard, D., Haines, T., Hall, P., Hellwing, W., Herenz, E. C., Hinton, S., Hlozek, R., Hoffman, J., Holman, D., Holwerda, B. W., Horton, A., Hummels, C., Jacobs, D., Juel Jensen, J., Jones, D., Karick, A., Kelley, L., Kenworthy, M., Kitchener, B., Klaes, D., Kohn, S., Konorski, P., Krawczyk, C., Kuehn, K., Kuutma, T., Lam, M. T., Lane, R., Liske, J., Lopez-Camara, D., Mack, K., Mangham, S., Mao, Q., Marsh, D. J. E., Mateu, C., Maurin, L., McCormac, J., Momcheva, I., Monteiro, H., Mueller, M., Munoz, R., Naidu, R., Nelson, N., Nitschelm, C., North, C., Nunez-Iglesias, J., Ogaz, S., Owen, R., Parejko, J., Patrício, V., Pepper, J., Perrin, M., Pickering, T., Piscionere, J., Pogge, R., Poleski, R., Pourtsidou, A., Price-Whelan, A. M., Rawls, M. L., Read, S., Rees, G., Rein, H., Rice, T., Riemer-Sørensen, S., Rusomarov, N., Sanchez, S. F., Santander-García, M., Sarid, G., Schoenell, W., Scholz, A., Schuhmann, R. L., Schuster, W., Scicluna, P., Seidel, M., Shao, L., Sharma, P., Shulevski, A., Shupe, D., Sifón, C., Simmons, B., Sinha, M., Skillen, I., Soergel, B., Spriggs, T., Srinivasan, S., Stevens, A., Streicher, O., Suchyta, E., Tan, J., Telford, O. G., Thomas, R., Tonini, C., Tremblay, G., Tuttle, S., Urrutia, T., Vaughan, S., Verdugo, M., Wagner, A., Walawender, J., Wetzel, A., Willett, K., Williams, P. K. G., Yang, G., Zhu, G., and Zonca, A.: 2016, *ArXiv e-prints*

Offringa, A. R., van de Gronde, J. J., and Roerdink, J. B. T. M.: 2012, *A&A* **539**, A95

Parsons, A.: 2016, *AIPY: Astronomical Interferometry in PYthon*, Astrophysics Source Code Library

Parsons, A., Pober, J., McQuinn, M., Jacobs, D., and Aguirre, J.: 2012a, *ApJ* **753**, 81

Parsons, A. R. and Backer, D. C.: 2009, *AJ* **138**, 219

Parsons, A. R., Liu, A., Aguirre, J. E., Ali, Z. S., Bradley, R. F., Carilli, C. L., DeBoer, D. R., Dexter, M. R., Gugliucci, N. E., Jacobs, D. C., Klima, P., MacMahon, D. H. E., Manley, J. R., Moore, D. F., Pober, J. C., Stefan, I. I., and Walbrugh, W. P.: 2014, *ApJ* **788**, 106

- Parsons, A. R., Pober, J. C., Aguirre, J. E., Carilli, C. L., Jacobs, D. C., and Moore, D. F.: 2012b, *ApJ* **756**, 165
- Paszke, A., Gross, S., Chintala, S., Chanan, G., Yang, E., DeVito, Z., Lin, Z., Desmaison, A., Antiga, L., and Lerer, A.: 2017
- Pober, J. C., Parsons, A. R., Aguirre, J. E., Ali, Z., Bradley, R. F., Carilli, C. L., DeBoer, D., Dexter, M., Gugliucci, N. E., Jacobs, D. C., Klima, P. J., MacMahon, D., Manley, J., Moore, D. F., Stefan, I. I., and Walbrugh, W. P.: 2013, *ApJL* **768**, L36
- Sault, R. J., Hamaker, J. P., and Bregman, J. D.: 1996, *A&AS* **117**, 149
- Sault, R. J., Teuben, P., and Wright, M. C. H.: 2011, *MIRIAD: Multi-channel Image Reconstruction, Image Analysis, and Display*, Astrophysics Source Code Library
- SKA Panel: 2012, *Expert Panel on Radio Quiet Zone and RFI Regulation Report*, Technical report, Square Kilometer Array, [https://www.skatelescope.org/wp-content/uploads/2012/06/79\\_Report\\_of\\_The\\_Expert\\_Panel\\_on\\_Radio\\_Quiet\\_Zone\\_and\\_RFI\\_Regulation.pdf](https://www.skatelescope.org/wp-content/uploads/2012/06/79_Report_of_The_Expert_Panel_on_Radio_Quiet_Zone_and_RFI_Regulation.pdf)
- Smirnov, O. M.: 2011, *A&A* **527**, A106
- Sotomayor-Beltran, C., Sobey, C., Hessels, J. W. T., de Bruyn, G., Noutsos, A., Alexov, A., Anderson, J., Asgekar, A., Avruch, I. M., Beck, R., Bell, M. E., Bell, M. R., Benthum, M. J., Bernardi, G., Best, P., Birzan, L., Bonafede, A., Breitling, F., Broderick, J., Brouw, W. N., Brüggen, M., Ciardi, B., de Gasperin, F., Dettmar, R.-J., van Duin, A., Duscha, S., Eislöffel, J., Falcke, H., Fallows, R. A., Fender, R., Ferrari, C., Frieswijk, W., Garrett, M. A., Gießmeier, J., Grit, T., Gunst, A. W., Hassall, T. E., Heald, G., Hoeft, M., Horneffer, A., Iacobelli, M., Juetten, E., Karastergiou, A., Keane, E., Kohler, J., Kramer, M., Kondratiev, V. I., Koopmans, L. V. E., Kuniyoshi, M., Kuper, G., van Leeuwen, J., Maat, P., Macario, G., Markoff, S., McKean, J. P., Mulcahy, D. D., Munk, H., Orru, E., Paas, H., Pandey-Pommier, M., Pilia, M., Pizzo, R., Polatidis, A. G., Reich, W., Röttgering, H., Serylak, M., Sluman, J., Stappers, B. W., Tagger, M., Tang, Y.,

- Tasse, C., ter Veen, S., Vermeulen, R., van Weeren, R. J., Wijers, R. A. M. J., Wijnholds, S. J., Wise, M. W., Wucknitz, O., Yatawatta, S., and Zarka, P.: 2013, *A&A* **552**, A58
- South African Civil Aviation Authority: 2008, *FLIGHT CALIBRATION DATES OF VOR's IN THE REPUBLIC OF SOUTH AFRICA*, Technical Report 25.6, Aeronautical Information Circular, <http://209.203.9.244/resource%20center/AIC'S/25.6.pdf>
- Staatskoerant: 2008, *South African Table of Frequency Allocations*, Technical Report 31264, ICASA, [http://thornton.co.za/resources/31264\\_890\\_complete-1.pdf](http://thornton.co.za/resources/31264_890_complete-1.pdf)
- Sullivan, I. S., Morales, M. F., Hazelton, B. J., Arcus, W., Barnes, D., Bernardi, G., Briggs, F. H., Bowman, J. D., Bunton, J. D., Cappallo, R. J., Corey, B. E., Deshpande, A., deSouza, L., Emrich, D., Gaensler, B. M., Goetze, R., Greenhill, L. J., Herne, D., Hewitt, J. N., Johnston-Hollitt, M., Kaplan, D. L., Kasper, J. C., Kincaid, B. B., Koenig, R., Kratzenberg, E., Lonsdale, C. J., Lynch, M. J., McWhirter, S. R., Mitchell, D. A., Morgan, E., Oberoi, D., Ord, S. M., Pathikulangara, J., Prabu, T., Remillard, R. A., Rogers, A. E. E., Rosh, A., Salah, J. E., Sault, R. J., Udaya Shankar, N., Srivani, K. S., Stevens, J., Subrahmanyam, R., Tingay, S. J., Wayth, R. B., Waterson, M., Webster, R. L., Whitney, A. R., Williams, A., Williams, C. L., and Wyithe, J. S. B.: 2012, *ApJ* **759**, 17
- Thompson, A. R., Moran, J. M., and Swenson, Jr., G. W.: 2017, *Interferometry and Synthesis in Radio Astronomy, 3rd Edition*
- World Aero Data: 2016, [http://worldaerodata.com/wad.cgi?nav=VICTORIA+WEST&nav\\_id=VWV&na](http://worldaerodata.com/wad.cgi?nav=VICTORIA+WEST&nav_id=VWV&na) website